Coastal Atmospheric Circulation around an Idealized Cape during Wind-Driven Upwelling Studied from a Coupled Ocean–Atmosphere Model

NATALIE PERLIN AND ERIC D. SKYLLINGSTAD

College of Oceanic and Atmospheric Sciences, Oregon State University, Corvallis, Oregon

ROGER M. SAMELSON

College of Oceanic and Atmospheric Sciences, and Cooperative Institute for Oceanographic Satellite Studies, Oregon State University, Corvallis, Oregon

(Manuscript received 8 February 2010, in final form 16 October 2010)

ABSTRACT

The study analyzes atmospheric circulation around an idealized coastal cape during summertime upwelling-favorable wind conditions simulated by a mesoscale coupled ocean–atmosphere model. The domain resembles an eastern ocean boundary with a single cape protruding into the ocean in the center of a coastline. The model predicts the formation of an orographic wind intensification area on the lee side of the cape, extending a few hundred kilometers downstream and seaward. Imposed initial conditions do not contain a low-level temperature inversion, which nevertheless forms on the lee side of the cape during the simulation, and which is accompanied by high Froude numbers diagnosed in that area, suggesting the presence of the supercritical flow. Formation of such an inversion is likely caused by average easterly winds resulting on the lee side that bring warm air masses originating over land, as well as by air warming during adiabatic descent on the lee side of the topographic obstacle. Mountain leeside dynamics modulated by differential diurnal heating is thus suggested to dominate the wind regime in the studied case.

The location of this wind feature and its strong diurnal variations correlate well with the development and evolution of the localized lee side trough over the coastal ocean. The vertical extent of the leeside trough is limited by the subsidence inversion aloft. Diurnal modulations of the ocean sea surface temperatures (SSTs) and surface depth-averaged ocean current on the lee side of the cape are found to strongly correlate with wind stress variations over the same area.

Wind-driven coastal upwelling develops during the simulation and extends offshore about 50 km upwind of the cape. It widens twice as much on the lee side of the cape, where the coldest nearshore SSTs are found. The average wind stress–SST coupling in the 100-km coastal zone is strong for the region upwind of the cape, but is notably weaker for the downwind region, estimated from the 10-day-average fields. The study findings demonstrate that orographic and diurnal modulations of the near-surface atmospheric flow on the lee side of the cape notably affect the air–sea coupling on various temporal scales: weaker wind stress–SST coupling results for the long-term averages, while strong correlations are found on the diurnal scale.

1. Introduction

Coastal wind regimes along the west coast of North America are dominated by a typical established large-scale pressure system during a summer season, as well as strongly influenced by local terrain and sea surface temperatures (SSTs) in the nearshore area. Terrain features are responsible for flow intensification downwind of major capes along the Oregon–California coastline. Compounding these wind variations are mesoscale boundary layer effects generated by air–sea interaction with coastal upwelling. These two phenomena are examined in this study using a coupled mesoscale ocean and atmosphere model. This work builds upon the previous studies in which the model coupling methodology has been described, tested on several 2D and 3D cases, and applied for simple coastal upwelling studies (Perlin et al. 2007; Warner et al. 2008).

Atmospheric flow intensifications downwind from coastal capes and points have been thoroughly studied

Corresponding author address: Natalie Perlin, College of Oceanic and Atmospheric Sciences, Oregon State University, 104 COAS Admin. Bldg., Corvallis, OR 97331-5503.
E-mail: nperlin@coas.oregonstate.edu

DOI: 10.1175/2010MWR3372.1

using a combination of satellite and aircraft observations as well as numerical weather modeling and idealized mesoscale simulations (Beardsley et al. 1987; Winant et al. 1988; Burk and Thompson 1996; Burk et al. 1999; Dorman et al. 2000; Koračin and Dorman 2001; Edwards et al. 2001, 2002; Perlin et al. 2004, 2007). Flow intensification is typically explained by applying hydraulic theory in the form of a controlled flow expansion wave or expansion fan, within the trans- or supercritical flow in the marine atmospheric boundary layer. Alternative compression bulges are often found on the windward side of the coastal promontories (Beardsley et al. 1987; Winant et al. 1988; Rogerson 1999; Samelson 1992). The intensity of these mesoscale phenomena, their spatial extents, and their effects on the coastal ocean circulation, however, show some uncertainty and variability in the nearshore area (~100 km), where coastal topography, the diurnal cycle, and the underlying sea surface temperature field complicate the analysis (Enriquez and Friehe 1995; Dorman et al. 2000; Bielli et al. 2002; Haack et al. 2001, 2008).

The Oregon–California coast is known to experience persistent northerly winds during summertime, which cause divergence of the upper-ocean Ekman layer and nearshore upwelling. Upwelling is often limited to distances of 10–50 km from shore in regions with relatively simple topography, but can be notably altered in strength and offshore location around major coastal promontories (Strub et al. 1991; Barth and Smith 1998; Barth et al. 2000; Perlin et al. 2004; Huyer et al. 2005; Castelao and Barth 2007). Colder upwelled water tends to stabilize the overlying marine boundary layer, which in turn acts to reduce the downward momentum flux and wind forcing of the coastal ocean (Vickers et al. 2001; Samelson et al. 2002; Bane et al. 2005; Skyllingstad et al. 2005, 2007; Perlin et al. 2007). Coupling between the upper ocean and low-level winds has been observed and reported on greater scales, and some attempts to quantify the relationship have recently been made (Chelton et al. 2001; Chelton 2005; Chelton et al. 2007; Haack et al. 2008; Song et al. 2009; Jin et al. 2009). However, the extent to which this coupling is significant in regions of strong wind–topography interaction in the nearshore region and its implication for upwelling development are yet to be determined.

Orographic obstacles such as mountains and mountain ranges may notably affect the lower-tropospheric structure when the predominant large-scale flow is in the cross-mountain direction. Lee troughs (dynamic or orographic troughs) are features known to occur on the downwind side of a topographic obstacle (Holton 1992; Oertel and Prandtl 2004). Its formation is most often explained dynamically by a redistribution of the potential vorticity in the cross-mountain flow or, thermodynamically, by the warming due to adiabatic compression of the sinking air on the lee side of the mountain range. Coastal topography could have such effects as well. However, coastal areas are notoriously hard to study and verify due to the complex interaction of multiscale wind regimes, involving large-scale synoptic flow, its orographic modulation, and strong diurnal dependence. A few studies considering lee trough or leeside low formation in coastal areas in different parts of the world have been conducted to study these complex interactions (Sturman and Tyson 1981; McKendry et al. 1986; Batt et al. 2002). These studies have called attention to the robust interaction of forcing mechanisms on different temporal and spatial scales.

The objectives of the present study are the following. First, to analyze an idealized coastal circulation in the presence of a coastal promontory using the two-way coupled ocean–atmosphere mesoscale model, with particular attention paid to the spatial and temporal features of the wind regime in the lower troposphere. Second, to identify differences in developing wind-driven coastal upwelling around the cape in the presence of dynamically varying wind forcing. And third, to determine the importance of the effects of air–sea coupling in the area surrounding the cape based on the relationships between wind stress, sea surface temperature, and their derivatives.

This paper is organized as follows. The models' basics and simulation design are described in section 2. Section 3 analyzes the temporal averages of the model results, as well as the diurnal modulations of the atmospheric regime. Section 4 presents and discusses the wind stress–SST coupling and statistics, which also includes an additional simulation with the fixed-SST condition in the atmospheric model. A summary and discussion conclude the manuscript in section 5.

2. Model setup

a. General model description

In our coupled code, the Naval Research Laboratory (NRL) Coupled Ocean–Atmosphere Mesoscale Prediction System (COAMPS) mesoscale model (Hodur 1997) is used as the atmospheric model, and the Regional Ocean Modeling System (ROMS; Shchepetkin and McWilliams 2005) is used as an ocean component. These two major components of the coupled code communicate and exchange data via the Model Coupling Toolkit (MCT; Larson et al. 2005; information online at http://www-unix.mcs.anl.gov/mct). A description of the model coupling approach and simple testing results are presented in Warner et al. (2008).

COAMPS is a three-dimensional atmospheric prediction system based on the fully compressible form of the nonhydrostatic equations, solved using a time-splitting

technique (Klemp and Wilhelmson 1978). The pressure solver involves the use of the Exner function, $\pi = (p/p_{00})^{R_d/C_P}$, where p and p_{00} are the pressure and reference pressure, respectively; R_d is the dry gas constant; and C_P is the specific heat at constant pressure. The Exner function is decomposed into a time-invariant mean state and a perturbation as follows: $\pi(x, y, z, t) = \overline{\pi}(z) + \pi'(x, y, z, t)$. The mean states are assumed to be hydrostatically balanced so that $\partial\overline{\pi}/\partial z = -g/C_P\overline{\theta}_V$, where g is the gravity acceleration and $\overline{\theta}_V$ is the virtual potential temperature of the mean state. The prognostic equation is then solved for the perturbation term. Subgrid-scale vertical mixing and turbulence are treated following Mellor and Yamada's (1974) 2.5-level scheme, which features prognostic equations for the turbulent kinetic energy (TKE) and diagnostic equations for second-order quantities such as fluxes of heat, moisture, and momentum. The model estimates of the planetary boundary layer (referred to in text hereafter as the modeled PBL reference heights) are based on the flux Richardson number, the ratio of buoyant production of TKE to shear production of TKE. The PBL reference height is determined as the lowest level where this ratio exceeds a critical value of 0.5. Surface fluxes are computed using a modified Louis parameterization (Louis et al. 1982), corrected using Tropical Ocean and Global Atmosphere Coupled Ocean–Atmosphere Response Experiment (TOGA COARE) data for water grid points as described by Wang et al. (2002). The Louis scheme uses polynomial functions (F_M, F_H) of the bulk Richardson number Ri_B to compute the surface flux momentum and sensible heat in the following way:

$$u_*^2 = a^2 u^2 F_M\left(\frac{z}{z_0}, \mathrm{Ri}_B\right) \tag{1}$$

and

$$u_*\theta_* = \frac{a^2}{R} u \Delta\theta F_M\left(\frac{z}{z_0}, \mathrm{Ri}_B\right), \tag{2}$$

where u_* is the friction velocity, θ_* is the surface-layer temperature scale, the a^2 term is the neutral drag coefficient, u is the wind speed at the reference elevation z, z_0 is the surface roughness, $\Delta\theta$ is the air–sea temperature difference, and R is the ratio of the transfer coefficient for heat to that of momentum (0.74). An expression similar to Eq. (2) is applied to compute the latent heat flux u_*q_* except using Δq in place of $\Delta\theta$, where q_* is the surface-layer humidity scale and Δq is the difference between the saturated specific humidity at sea temperature and the air specific humidity at the reference level. Surface roughness computations in COAMPS include friction velocity variations and are based on Fairall et al. (1996).

The radiative transfer parameterization includes methods of short- and longwave radiative transfers through the atmosphere following Harshvardhan et al. (1987). Stratiform and cumulus clouds are the two types of clouds considered in the radiative transfer calculations; fractional coverage of stratiform clouds is diagnosed with critical values of relative humidity at each model level, and fractional coverage of cumulus clouds is diagnosed by means of the convective rainfall rate and temperature. Calculations of longwave radiation consider its absorption by water vapor, carbon dioxide, and ozone, computed by a broadband method of four band regimes; clouds are considered blackbodies in the longwave radiation scheme. Calculations of the shortwave radiation consider absorption by water vapor and ozone, as well as the multiple scattering of shortwave radiation in cloudy and clear skies.

The explicit moist physics in COAMPS consists of a single-moment bulk prediction of mixing ratios of five microphysical variables developed by Rutledge and Hobbs (1983) based on a bulk cloud model by Lin et al. (1983). Our simulations compute the following two microphysical variables: cloud and rain liquid water ratios. A subgrid-scale convective parameterization package in COAMPS is not used in current simulations, as was set up to be applied for horizontal grid dimensions greater than 9000 m; our current model grid size is below that limit.

The ROMS ocean component is a free-surface, terrain-following hydrostatic model, based on primitive equations solved using a split-explicit time-stepping scheme, separating barotropic (fast) and baroclinic (slow) modes (Shchepetkin and McWilliams 2005). For our study, vertical mixing is parameterized using the Mellor–Yamada 2.5-level scheme. Horizontal harmonic mixing is chosen to be computed along vertical levels for momentum and two tracers (temperature and salinity). Both COAMPS and ROMS utilize an Arakawa C grid, where spatial horizontal momentum points (u, v) are staggered relative to the mass points ρ, and all of the above are vertically staggered relative to the vertical momentum component w. This facilitates the numerical algorithms for the momentum and mass–tracer equations.

b. Experiment design

The horizontal model domain sizes are 310×410 points in the latitudinal and longitudinal directions, respectively, and both ocean and atmosphere models use 3-km grid boxes. The domain represents an eastern ocean boundary with a straight coastline having a single cape (Fig. 1a). The cape is represented in the center of the domain by two successive linear coastal bends, angling about 26.6°, similar to the value used in Burk et al. (1999). The cape extends seaward for 90 km, and has an alongshore extent of about

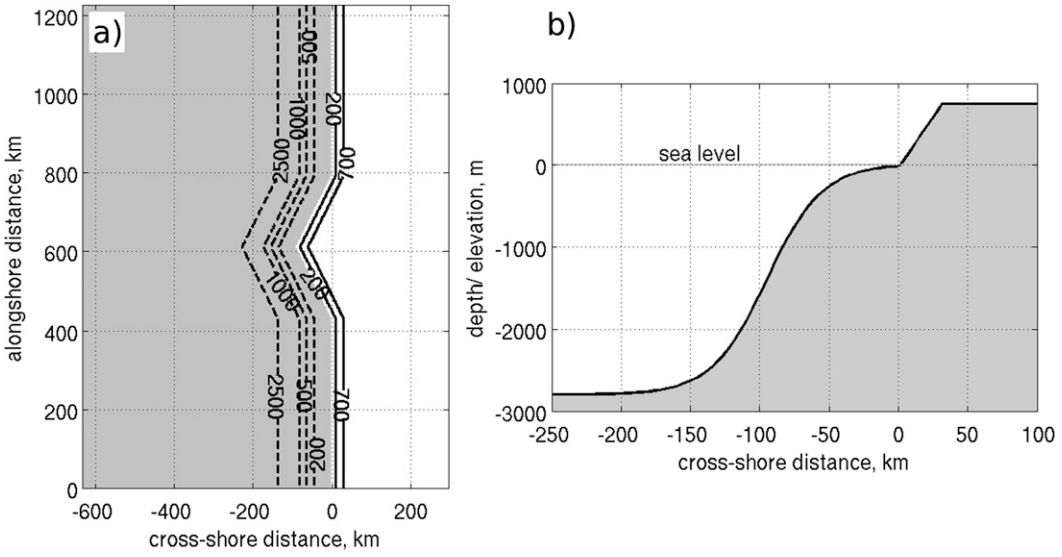

FIG. 1. (a) Bathymetry (m, dashed) and topography (m, solid) of the model domain featuring a coastal promontory (idealized cape). (b) Vertical view of the topography in the cross-shore direction. Topographical maximum is 750 m, and the land remains flat eastward upon reaching 750 m. Maximum depth is 2835 m, and the ocean bottom remains flat westward of that value.

350 km. The bathymetry for the simulations was approximated using a smooth continuous function to reflect the average dimensions of the continental shelf and shelf break off the Oregon coast, followed by the open-ocean offshore region with a depth of 2835 m (Fig. 1b). Along the northwest Pacific coast, land topography varies from about 350 m (on average) along the central Oregon coast, to approximately 2000 m for the coastal mountains in northern California. In our model setup, the land topography increases eastward at a rate of 25-m elevation per 1-km horizontal distance, and remains flat in the eastward direction upon reaching 750 m.

Both the atmospheric and ocean models adopt a terrain-following sigma coordinate system in the vertical direction. The atmospheric model has 47 vertical sigma levels stretched from the ground up to 9300 m, with 15 levels below 200 m, aimed to better resolve air–sea coupling effects. The ocean model has 40 vertical sigma levels with the vertical grid spacing concentrated near the surface and bottom. Horizontally homogeneous model initialization is applied based on vertical profiles of the potential temperature and water vapor mixing ratio for the atmosphere, and temperature and salinity for the ocean (Fig. 2). The initial atmospheric temperature profile is linearized using the typical summer values, but no atmospheric boundary layer is prescribed, allowing it to develop dynamically according to the model surface and atmospheric conditions during the simulation. The atmospheric wind is initially set to match the 15 m s^{-1} geostrophic northerly flow in the lowest 1.5 km, decreasing to 5 m s^{-1} above between 1.5 and 2 km. A geostrophic pressure gradient is determined from this imposed flow and is used as a constant term in the momentum balance equations. To account for a typical summertime subsidence pattern in the eastern Pacific region, incremental heating of the atmospheric profile is added at a rate of 1°C day^{-1}. Ocean stratification (Fig. 2b) is imposed at the beginning of the simulation, being largely determined by seasonal variability. Simulations start with the ocean at rest in order to follow the development of the coastal upwelling in response to the dynamically varying wind forcing.

Special attention is given to the choice of boundary conditions due to the 11.5-day duration of the simulations, which is an unusually long period for a mesoscale atmospheric model to run in an idealized mode. Periodic north–south boundary conditions are employed in both the ocean and atmospheric models. Lateral boundary conditions for the ocean model consist of a coastal wall on the east, with radiation for momentum and tracers and gradient conditions for the free surface along the western boundary. In the atmospheric model, eastern and western lateral boundaries use radiation conditions that distinguish between inflow and outflow points. At inflow points, all boundary variables are set to their initial values. At outflow points, the normal velocity out of the domain v_n is computed using the upstream differencing method of Miller and Thorpe (1981). The general approach of the radiation condition is to ensure that $\partial v_n/\partial t + \hat{c}(\partial v_n/\partial n) = 0$. Here, $\hat{c}$ is a velocity that includes wave propagation and advection $\hat{c} = -(v_n + c^*)$ where c^* is the phase speed for

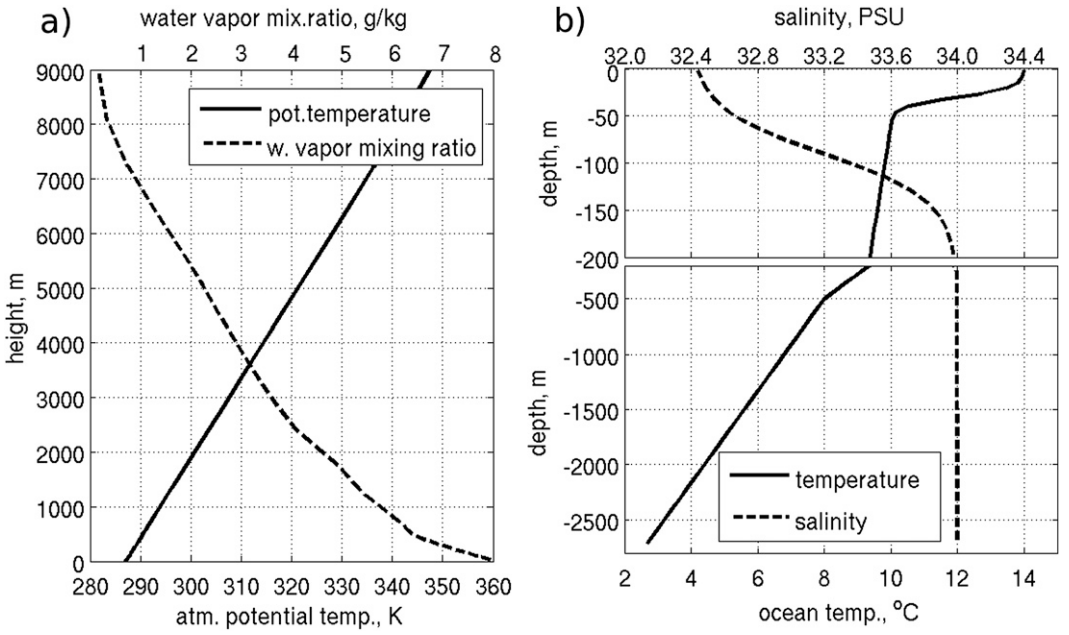

FIG. 2. Initial vertical profiles of atmosphere and ocean model variables: (a) atmospheric potential temperature (K, solid line) and water vapor mixing ratio (g kg^{-1}, dashed line) and (b) ocean temperature (°C, solid) and ocean salinity (PSU, dashed). Note the composite scale that highlights the upper-ocean structure: (top) 0–200- and (bottom) 200–2500-m depths.

fastest-moving gravity waves directed out of the domain. In the model, boundary values of v_n at the next time step, v_b^{t+1}, are estimated from boundary values at time step t, v_b^t, and the value one grid point inside of the boundary at the same time step v_{b-1}^t following

$$v_b^{t+1} = v_b^t - (\hat{c}\Delta t/\Delta x)(v_b^t - v_{b-1}^t), \tag{3}$$

where Δt and Δx are the model time step and grid spacing in the direction normal to the boundary, respectively. The modified gravity wave speed $\hat{c}$ is either set to be constant, or is estimated at time step t by solving Eq. (3) with respect to $\hat{c}$ and applying velocities at one and two grid points from the boundary at the preceding time step, v_{b-1}^{t-1} and v_{b-2}^{t-1}, respectively. All other variables, except the velocity normal to the boundary, are linearly extrapolated at outflow points. This approach is similar for both the western and eastern boundaries, while $(b - 1)$ and $(b - 2)$ refer to the first and second points from the boundary toward the model domain.

The time steps in the two models are 10 s in the atmospheric model and 300 s in the ocean model, with a data exchange occurring on the ocean model time step. The ocean receives momentum flux, net heat flux, and solar radiation from the atmospheric model averaged over the data exchange time period. In return, the atmospheric model receives SST computed by the ocean model at each time step. Simulations are conducted for 276 h, allowing 36 h for the coupled model spinup and following 240 h (10 days) of forecast time used in analyzing the results.

3. Coastal ocean wind stresses and the lower-atmospheric regime

a. Temporal means of surface quantities

The modeled wind stress vectors and magnitude, 10-m wind speed and wind components, and mean surface pressure, averaged over the 10 days of the coupled simulation, are shown in Figs. 3a–c. Mean wind stress vectors are oriented south-southeastward, stemming from the northerly geostrophic flow rotated within the atmospheric Ekman layer. A broad wind stress maximum stretches downwind and seaward from the point of the cape 300–400 km offshore, as traced by the 0.2 N m^{-2} and 13 m s^{-1} contours. A surface pressure map indicates a local trough formed on the downwind side of the cape; the area of lowest pressure approximately corresponds to the location of a leeside wind feature.

Average wind stresses and winds are notably lower within ~50 km of the coast along the straight coastline and upwind of the cape, up to 2–3 times their offshore values. This nearshore wind reduction primarily results from the atmosphere response to ocean upwelling that develops during the simulation (discussed further in the text below). North of the cape, wind deceleration gradually occurs 200–300 km upwind and extends 150–200 km offshore. This

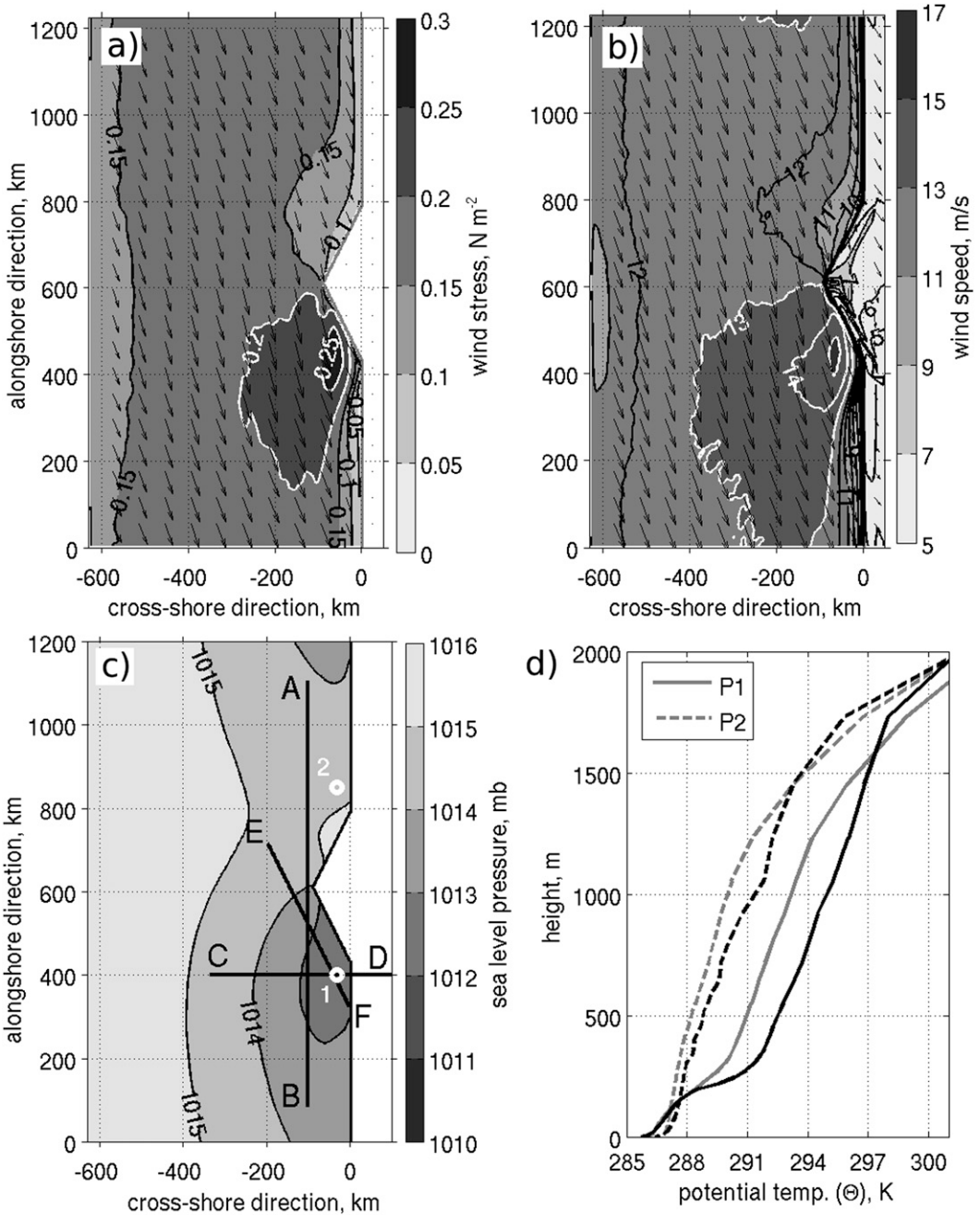

FIG. 3. (a) Mean wind stress components and magnitude (N m^{-2}) from the coupled simulation, averaged for 10 days (forecast hours 37–276), (b) mean 10-m wind components and speed (m s^{-1}) for the same 10-day period, (c) mean sea level pressure (mb) for the same 10-day period, and (d) potential temperature profiles at two locations marked 1 and 2 in (c), for the final simulation time (1700 LST, black) and for 10-day averages (gray). Hourly means of the wind stress components were computed using the values at each time step of the atmospheric model. A wind stress magnitude was computed for each hour from the corresponding hourly means of its components, and then averaged over 10 days. The average 10-m wind speed was computed from hourly model output of the instantaneous values of wind components. Vectors are plotted every 20th point of the model grid to avoid clutter. Black lines in (c) indicate the A–B, C–D, and E–F transects presented in subsequent figures.

upwind feature has a corresponding weak ridge in the surface pressure field. At the same time, a weak east–west surface pressure gradient is present along the entire domain, in agreement with north-northwesterly offshore winds. The potential temperature profiles at the final time of the simulation (Fig. 3d, black lines) demonstrate the difference in the marine boundary layer structure on both sides of the cape: a low-level temperature inversion at 200–250-m height forms on its lee side only. This inversion slightly varies in strength and height during the course of the day, but nonetheless is present at all times. Due to diurnal variations of the potential temperature within the lowest ~1500 m over the leeward location, this low-level inversion is not so apparent on the temporally averaged profile (gray line). No low-level inversion forms on the windward side of the cape. The mechanisms for the inversion formation are discussed further in the text below.

Persistent north-northwest winds over the domain force coastal upwelling that transports colder water to the ocean surface in the nearshore region (Fig. 4a). The initial SST is 14°C and increase about 1°–2°C due to solar radiative heating, whereas nearshore temporally averaged SSTs show a decrease by 2°–4°C from the initial value, depending on their relative location around the cape. The coldest SSTs are found in the nearshore region of the downwind side of the cape. The temperature difference of about 4°C across the 50 km nearest the shore is a typical value for the Oregon coast during the summertime upwelling season (Huyer et al. 2005). Persistent wind forcing produces a surface ocean coastal jet directed southward along the coast, with the strongest surface currents resulting over the midshelf (between 90- and 400-m depth). Another spatial feature of the nearshore SST field is a set of small-scale ocean eddies that develop along the cape's coastline. In particular, a closed cyclonic ocean eddy that is tens of kilometers in size formed westward of the cape tip, and several eddy-like structures of similar size formed along the leeside coast. These smaller eddies are not as evident in the average SST field or ocean surface current plot, but are more apparent in the close-up view (not shown). A separate manuscript focusing on an analysis and discussion of the coastal ocean circulation pattern from this case study is currently in preparation.

The average modeled PBL reference heights and Froude number, computed as described below, are shown in Fig. 4b. The Froude number estimates the possibility of the upstream propagation of gravity waves, and is defined as $\mathrm{Fr} = \overline{V}(g'H)^{-1/2}$, which includes the marine-layer depth H below the inversion; the reduced gravity, $g' = g\Delta\theta/\overline{\theta}$, where $\overline{\theta}$ and $\overline{V}$ are the marine layer potential temperature and wind speed, respectively; and $\Delta\theta$ is the temperature jump across the inversion. The base and top of the inversion are estimated from the potential temperature profile [method described in Burk and Haack (2000), p. 1445; Haack et al. (2001), p. 694], where the marine-layer depth H is taken as being midway between the base and the top of the inversion, whereas $\overline{\theta}$ and $\overline{V}$ are vertically averaged between the surface and H.

Modeled PBL reference heights notably vary across the domain, and especially so downwind of the cape (Fig. 4b). Average values for the 10-day period are about 500–550 m in the offshore direction and away from the western boundary. Their gradual reduction to 300–400 m also occurs in the vicinity of the land–ocean boundary, approximately corresponding to the offshore extent of the upwelling zone (cf. Fig. 4a), and where the wind stresses fall below 0.1 N m^{-2}. On the lee side of the cape, however, the modeled PBL reference height decreases rapidly nearshore, dropping below 200 to 100 m near the coastline, with an almost twofold decrease occurring over short alongshore or cross-shore distances. This TKE-based estimates of the PBL reference height on the lee side correspond well with the formation of a lower-level inversion shown earlier in Fig. 3d. Elevated Froude numbers (greater than 1) in the same region as the decreased model PBL reference heights suggest the presence of a supercritical flow on the leeward side.

The spatial correlation of the mean SST and modeled PBL reference heights (Figs. 4a and 4b) within 200 km off the coast is 0.77. Some of this correlation arises because the strongest winds, and thus the strongest local upwelling response, are also found in the area of wind intensification on the lee side of the cape where the modeled PBL reference height is shallow. Air–sea boundary layer coupling, as discussed below, also accounts for a portion of the high correlation.

Some aspects of the spatial patterns of mean sensible and latent surface heat flux (positive upward), averaged over 10 days (Figs. 4c and 4d), are related to the upwelling-modified SST. Over most of the ocean domain, sensible (latent) heat fluxes are slightly negative (positive). Lowest sensible heat fluxes are found near the tip of the cape and along the coast of its southern side, reaching -40 W m^{-2}, while the latent heat fluxes become negative and reach below -20 W m^{-2} over the same area. A narrow zone of negative latent heat fluxes that stabilize the atmosphere is found over most of the nearshore upwelling area. The presence of areas with negative latent and sensible heat fluxes downwind of capes along the U.S. west coast has been reported by observational studies as well (Fig. 14 in Edwards et al. 2001; Fig. 4 in Haack et al. 2005).

b. Mean vertical structure of the lower troposphere

Analysis of the mean vertical structure of the lowest troposphere developed during the simulation is shown

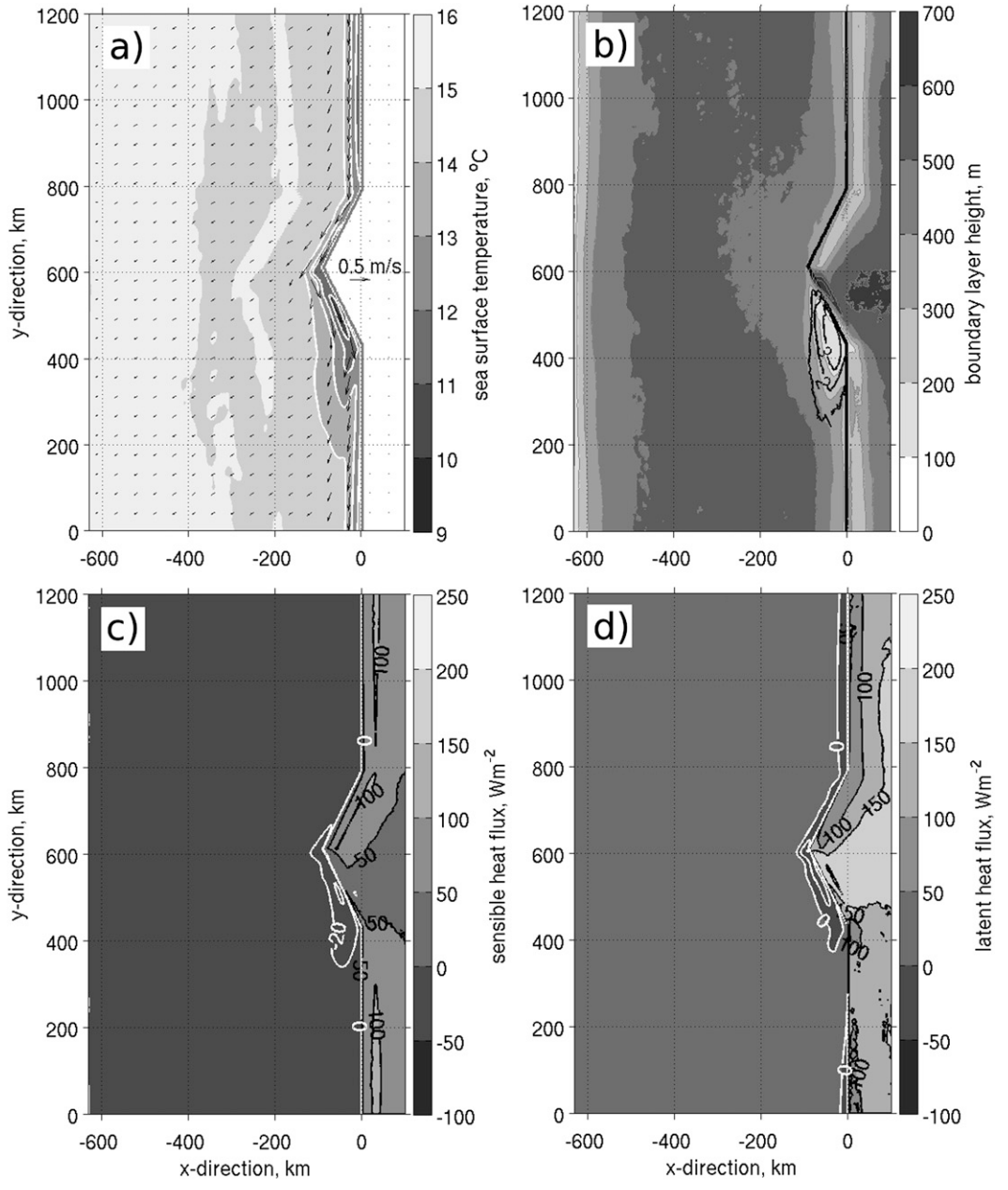

FIG. 4. Coupled simulation results, averaged for the same 10-day period as in Fig. 3: (a) SSTs (°C, shaded) overlaid by ocean surface u- and v-velocity components (m s^{-1}, vectors), (b) modeled PBL reference heights (shading, m) and average Froude number (contours, nondimensional), (c) sensible heat fluxes, and (d) latent heat fluxes (W m^{-2}). Contours for surface fluxes are −40, −20, 0, 50, 100, 150, and 200. Ocean surface velocity components are plotted every 15th grid point. All variables were computed using hourly model outputs. See text for details on Froude number computation.

in the alongshore (A–B line) and cross-shore (C–D line) directions of the average model quantities (Figs. 5 and 6). In addition to the leeside trough formation shown earlier (Fig. 2c), an orographic influence on the flow is evidenced by southward wind component acceleration around the cape in the alongshore cross section (Fig. 5a). An elevated northerly jet is found along the coastline, peaking near the modeled PBL reference height. This jet intensifies leeward of the cape; and the strongest values of the elevated wind maximum are found more than 100 km away from the coastline (Fig. 6a). The mechanism behind the formation of a 2D alongshore low-level jet (LLJ) is similar to the one described by Burk and Thompson (1996). The averaged westerly wind cross sections (Figs. 5b and 6b) indicate a wind increase within the modeled PBL reference heights, and

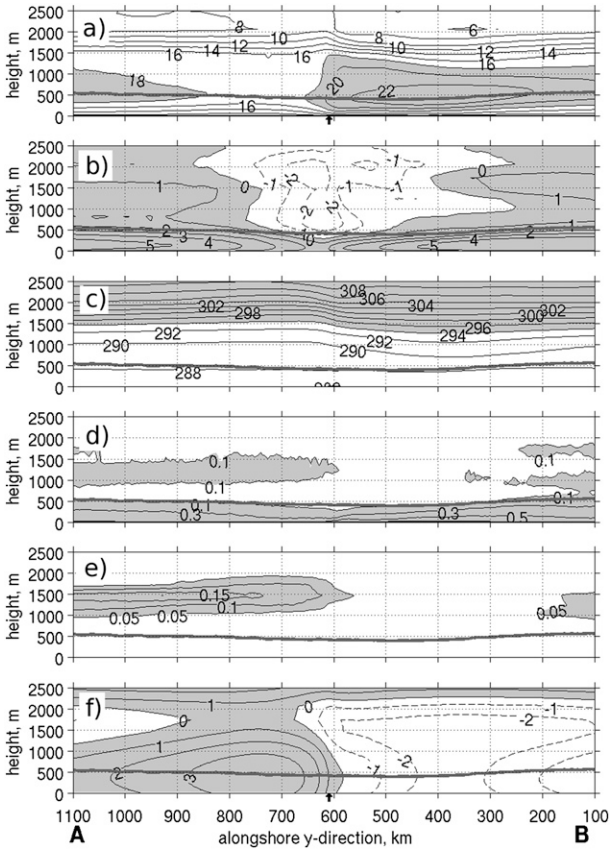

FIG. 5. Vertical cross sections along the A–B transect (indicated in Fig. 3c) of the 10-day averaged modeled quantities: (a) southward component of the horizontal wind (positive southward, m s^{-1}, shaded >18 m s^{-1}), (b) easterly wind component (m s^{-1}, positive values shaded), (c) potential temperature (K, shaded >294), (d) turbulent kinetic energy (m^2 s^{-2}, shaded >0.1), (e) cloud water mixing ratio (g kg^{-1}, shaded >0.05), and (f) perturbation Exner function (nondimensional, $\times 10^4$, positive values shaded). Dark gray lines in all the panels indicate modeled PBL reference heights (m) for the same averaging period. Shading is applied to highlight field structures. Traverse of the point of the cape is marked by small black arrows in the top and bottom panels, at about $y = 610$ km.

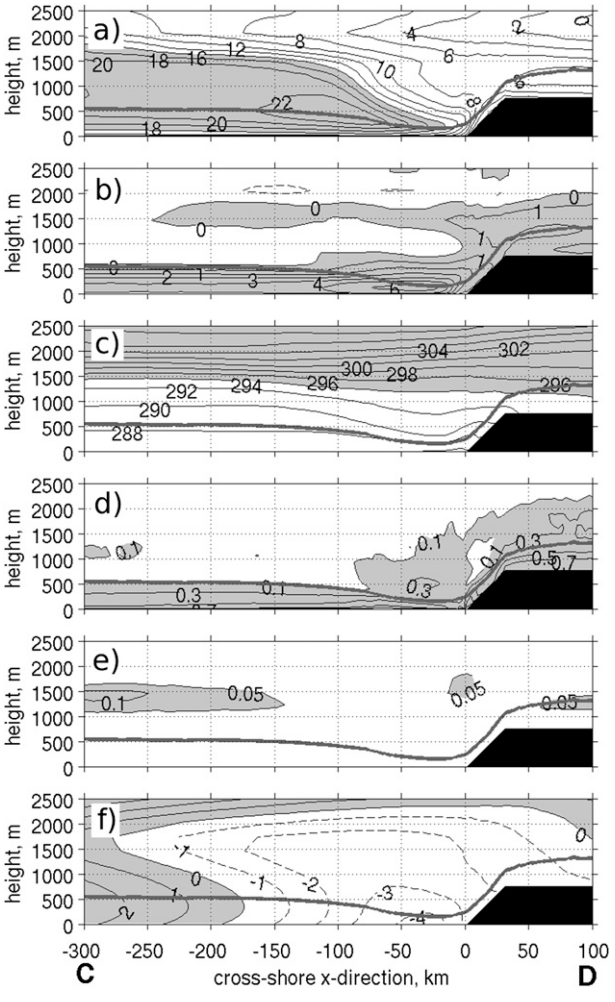

FIG. 6. As in Fig. 5, but for the C–D transect.

the location of the wind maximum on the lee side within 50–100 km of the coast. The distinction in the seaward location of the elevated wind maxima of the two horizontal wind components (Fig. 6) may indicate differences in the dynamical forcing or temporal scales responsible for producing these maxima. In the vicinity of the cape, an elevated region of easterly winds (Fig. 5b) may indicate that the arriving air masses originate over the land (cape) and are warmer than the ambient marine layer profile, warming the air column on the lee side of the topographic obstacle. Easterly winds are even stronger for the locations inshore of the A–B cross section, and reach 3–4 m s^{-1} (not shown). This is consistent with potential temperature profiles in Fig. 3d that show a low-level inversion with a warmer layer above 200 m at a leeward location.

Average potential temperature profiles (Figs. 5c and 6c) suggest neutral or very weak stratification of the lower troposphere above the ocean, with the subsidence inversion found between 1500 and 2000 m. Isentropes are slightly doming on the windward side and sloping downward on the lee side (Fig. 5c), and also sloping toward the land (Fig. 6c). The temperatures are warmer on the lee side than north of cape throughout most of the air column below the subsidence inversion. Possible mechanisms for this heating are the westward advection of air from the land, as discussed above, as well as likely adiabatic decent of air downwind of a topographic obstacle. A minimum in the potential temperature, however, results in the lee side over cool upwelled water near the coast, where temperatures as low as 286 K are found, suggesting the development of an internal boundary layer.

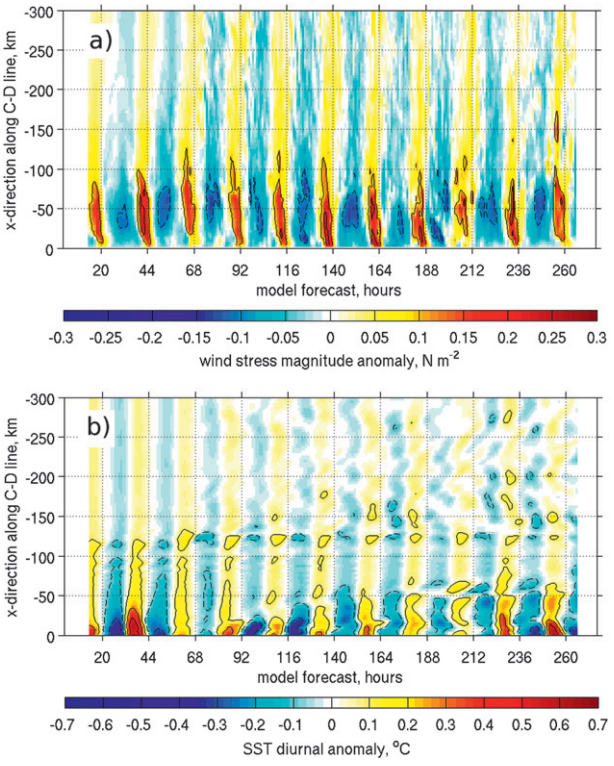

FIG. 7. Hovmöller diagram showing the evolution of the diurnal anomalies of (a) wind stress magnitudes and (b) SSTs (°C), along the C–D transect indicated in Fig. 3c. The anomalies are computed by subtracting the corresponding 24-h running averages from the modeled values. Contours are −0.1, 0.1, 0.2, and 0.3 for the wind stresses, and −0.5, −0.3, −0.1, 0.1, 0.3, and 0.5 for the SST anomalies. Tick marks along the *x* axis correspond to midnight (0000 LST) of each day.

Away from the coastline, the highest parameterized turbulence kinetic energy values occur near the ocean surface, where they provide a measure for the modeled PBL reference height estimate (Figs. 5d and 6d; TKE isoline of 0.1 $m^2 s^{-2}$). The TKE increase within the lowest 1000 m on the lee side of the cape could be explained by strong vertical wind shear in that region. The cross-shore cross section gives an indication of some TKE decrease within ~20 km of the coast (Fig. 6d), which is even more pronounced when the cross section is moved 100 km to the south (not shown). A nearshore TKE decrease is associated with the increased stability of the boundary layer over the cold water. Higher cloud water mixing ratios result along the windward side of the cape, with nearly cloud-free areas in the 150-km nearshore area on the lee side (Figs. 5e and 6e). Although the cloud formation is very dynamical and transient, varying both in space and time of the day in our simulation, the average result is very consistent with the observations. Cloud-free regions on the lee side of coastal capes, as well as stronger cloud formation on the windward side of capes and on windward slopes of coastal topography, are often observed over the eastern Pacific coast (e.g., Fig. 1 in Haack et al. 2001). An elevated turbulence layer is higher over the land, and extends about 1500 m above the ground, whereas the cloud layer remains at lower levels (Figs. 6d and 6e). This likely occurs due to time averaging, because the boundary layer above the ground is highly dynamic due to strong land surface warming. The temporal average of the TKE could therefore be indicative of the diurnal extent of the boundary layer depth, whereas the average cloud layer is indicative of the average level where stratiform clouds and fog are formed during the evening and night boundary layer decay and stabilization in the lower levels. Notably lower modeled PBL reference heights over the land result on the windward side of the coastal topography, in contrast to the regions farther inland, and likely occur due to the advection of the cool marine layer (note the average westerly flow).

The Exner function perturbations from the mean state (Figs. 5–6f) are indicative of pressure perturbations, and are consistent with the average surface pressure field (Fig. 3c), in reporting decreased pressure on the lee side of the cape, and a pressure increase on the windward side. In the vertical direction, the pressure perturbation minimum is located at the base of the subsidence inversion, whereas the maximum is found at the modeled boundary layer top. A pressure redistribution pattern could be an illustration of the momentum flux convergence (divergence) on the windward (lee) side of the topographic obstacle. Additional analysis of the momentum budget, turbulence, and stability will be reported upon in a separate publication focusing on the atmospheric circulation.

c. *Diurnal variations*

Diurnal heating and cooling of the land causes a strong daily cycle of the surface heat fluxes and the modeled PBL reference heights over land, in comparison with their notably smaller variations over the coastal ocean. When combined with coastal promontories and the local topography, a significant diurnal cycle results over the coastal ocean on the lee side of the cape as well. Hovmöller diagrams of wind stress and SST anomalies along the C–D and E–F transects illustrate the range of diurnal variations (Figs. 7 and 8). To separate the diurnal amplitudes from longer-term trends, the time series results are high-pass filtered, which involves computing the anomalies of the modeled time series from their corresponding 24-h running averages. The peak in diurnal wind stresses along the C–D transect occurs a few hours before midnight and is very brief. Strongest diurnal amplitudes of over 0.30 N m^{-2} are found 20–50 km away from the coast (Fig. 7a). The diurnal amplitudes of SSTs are usually the strongest near the coast and in the southern part of the cape, where they

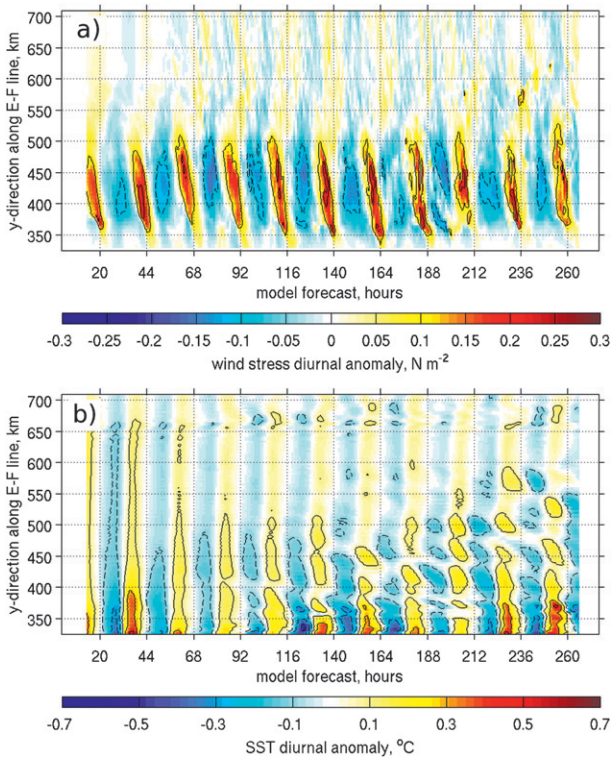

FIG. 8. As in Fig. 7, but for the E–F transect. Note that the *y* axis corresponds to distances in the *y* direction of the model grid, and not to linear distances along the transect.

reach 0.8°C. Positive SST anomalies are always found between local noon and midnight, peaking in the afternoon hours. The highest diurnal variations in wind stress magnitudes along the E–F transect are found primarily along the southern part of the cape, where the amplitudes reach 0.3 N m^{-2} (Fig. 8a). Wind and the wind stresses peak in the evening and early night hours; the local diurnal wind stress maximum appears to be propagating downstream along the coastline, between $y = 500$ and 350 km.

To evaluate the spatial structure of the modeled fields over the course of the day, 10-day averages of modeled wind stress and surface pressure are computed for the specific hours of the day, further referred to as "morning" (0600 LST), "daytime" (1200 LST), "evening" (1800 LST), and "night" (0000 LST), and presented in Fig. 9. Upstream of the cape, wind stresses are the weakest during the daytime and strongest at night; a daytime decrease in wind stresses also corresponds to a strengthening of the surface pressure ridge on the windward side of the cape. On the lee side of the cape, the timing of wind stress extremes depends on downstream and offshore locations. In the near-shore, they are ~50 km from the coast, the weakest wind stresses occur during the morning and are accompanied by a shallower lee trough. The lee trough deepening starts during daytime, and wind stresses then increase in the nearshore region on the downwind side. The strongest wind stresses occur during the evening hours along with a deeper lee trough southwest of the leeward side of the cape. Farther offshore, away from the localized wind stress maximum, the wind stresses are strongest (weakest) during nighttime (daytime).

The presence of strong diurnal variations in the coastal ocean along the U.S. west coast, and in particular around the coastal capes, has been found by both observational and modeling studies (Beardsley et al. 1987; Burk and Thompson 1996; Kindle et al. 2002; Bielli et al. 2002; Perlin et al. 2004; Haack et al. 2008). The combination of orographic and diurnal effects is likely the source of the reported variability in the coastal region, but the exact mechanism responsible for the diurnal variations has yet to be determined. The range and spatial scale of diurnal variations in our coupled simulation could be studied using Fig. 10, from the average anomalies of the wind stress, surface pressure, and SST for the four distinct times of the day. The most prominent feature in the wind stress anomalies is their greatest amplitudes on the lee side of the cape that could exceed 0.3 N m^{-2}, similar to the estimates from Fig. 8a. The highest wind stress anomalies over the area extending southwestward from the lee side of the cape occur during the evening, and the wind stresses are weakest in the morning. Elsewhere in the domain, the strongest (weakest) wind stress anomalies occur at night (during the daytime). Offshore wind stress diurnal amplitudes are around 0.05 N m^{-2} or less. The occurrences of wind stress extremes on the lee side of the cape correspond well with the surface pressure anomalies, in which deepening (shallowing) of the lee trough results in the evening (morning). Diurnal variation of surface pressure on the lee side of the cape is the major spatial feature of the anomaly field. Note that the deepest pressure anomaly is found on the southern edge of the cape, and it relaxes farther downstream.

SST anomalies are shown to be the strongest on the lee side as well, but its average nearshore spatial features are more irregular (Fig. 10, bottom row), likely due to the developing nearshore ocean eddies mentioned earlier. The SST diurnal peaks occur during the evening, and the lowest SSTs occur during morning times. In the 50-km nearshore zone of the downwind coast of the cape, an irregular pattern of warm (cold) SST anomalies appears during the daytime (nighttime), earlier than the domain-wide maximum (minimum). This early onset of warmer (colder) nearshore temperatures approximately corresponds to positive (negative) wind stress anomalies during the daytime (nighttime) off the downwind side of the cape.

Correlations between the time series of diurnal anomalies in wind stress and surface pressure, SST, and 20-m

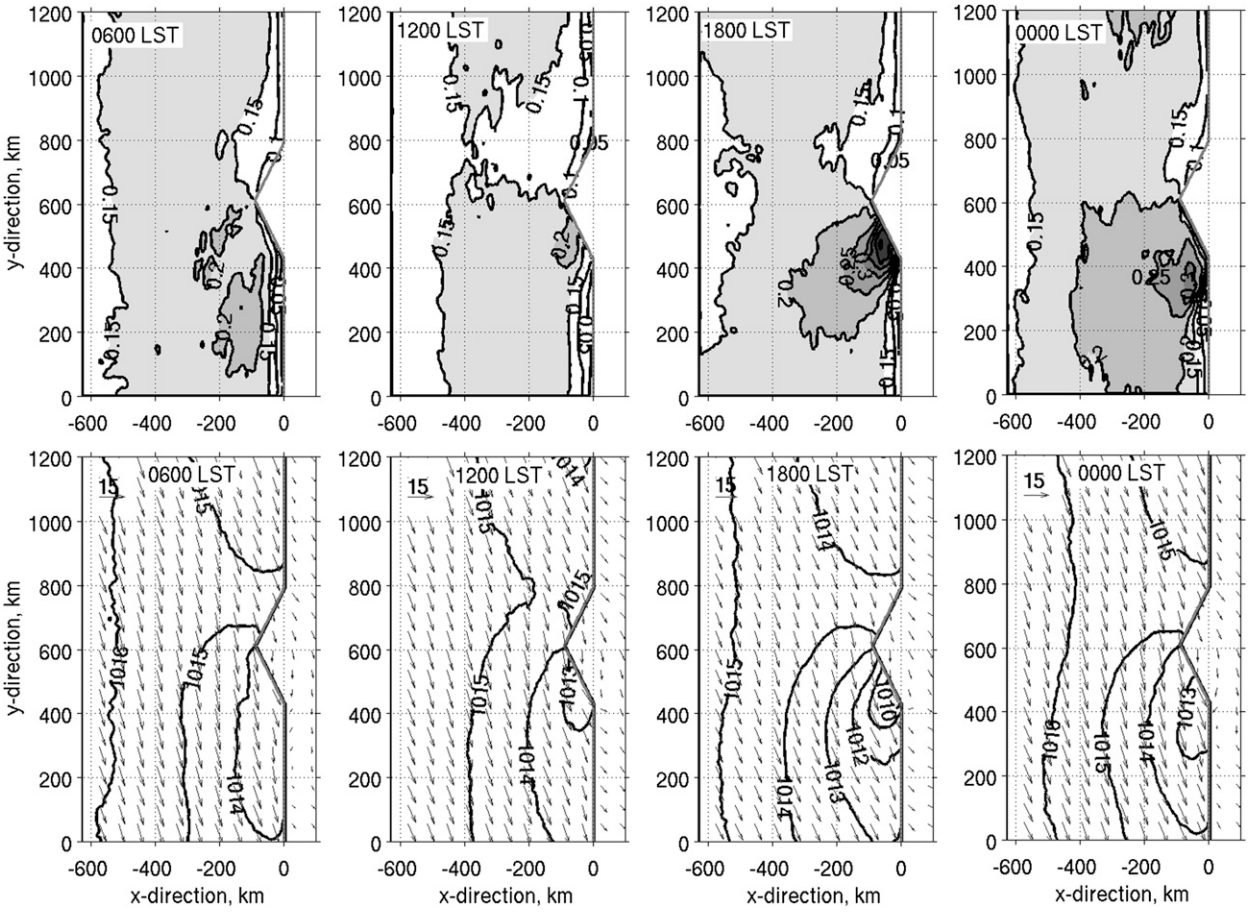

FIG. 9. (top) Wind stress magnitude and (bottom) surface pressure and 10-m wind components, averaged for 10 days for (left to right) the following hours (LST): 0600 (morning), 1200 (daytime), 1800 (evening), and 0000 (night). Time is indicated at the top of each panel. Contour intervals are 0.05 N m^{-2} for the wind stress and 1 mb for the pressure.

depth-averaged ocean current are shown in Fig. 11. The most prominent feature in these plots is the large zone of high negative or high positive correlations for the shown variable pairs (greater than 0.5 in absolute values), stretching southwestward more than 200 km offshore of the lee side of the cape. Note that the extent of the ocean response to the diurnal forcing in both SST and depth-averaged surface current (Figs. 11b and 11c) is similar to the extent of the pressure variations. The stronger correlation on a diurnal scale between the wind stresses and ocean currents on the lee side is quite remarkable, as it does not directly involve diurnal heating effects, as in the case of SSTs.

4. Wind stress and SST relationships and statistics

a. Coupled-case analysis

Analyses of SST–stress coupling such as that of Chelton et al. (2001) are focused on three primary quantities: the correlation of wind stress and SST, of wind stress curl and crosswind SST gradient, and of wind stress divergence and downwind SST gradient. The overlay of time-averaged fields of wind stress and SST, and their derivatives, provides an initial estimate of the correspondence between these fields. The spatial features of the average SSTs and wind stresses (Fig. 12a) are well matched upwind of the cape and far downstream near the southern domain boundary, and notably differ on the lee side of the cape. Based on these major spatial features, we subdivide the domain into the following two regions for further analysis. The ''upwind region'' includes alongshore 400 km north of the tip of the cape ($y = 610$ km), and the ''downwind region'' includes 400 km south of the tip.

Time averages of wind stress curl $[\mathbf{k} \cdot (\nabla \times \tau) = (\partial\tau_y/\partial x) - (\partial\tau_x/\partial y)]$ and wind stress divergence $[\nabla \cdot \tau = (\partial\tau_x/\partial x) + (\partial\tau_y/\partial y)]$ are shown in Fig. 12, and are overlaid by the crosswind SST gradient (CWSST) and downwind SST gradient (DWSST), respectively. The averaging

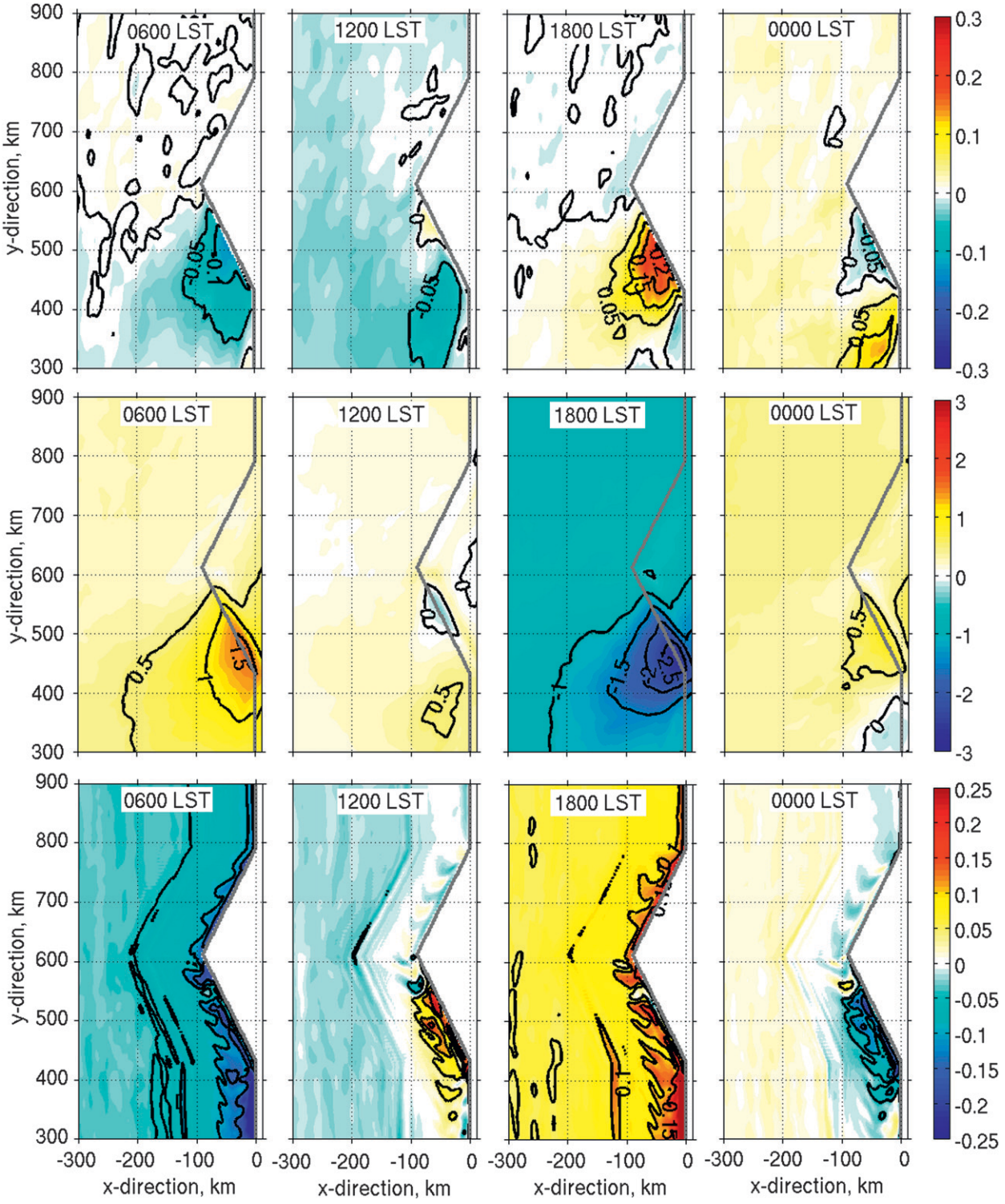

FIG. 10. Ten-day-average anomalies from the corresponding 24-h running means of the (top) wind stress magnitudes (N m^{-2}), (middle) surface pressure (mb), and (bottom) SST (°C), for (left to right) the four distinct times of the day (see Fig. 9). SST difference contours are −0.15, −0.1, −0.05, 0.05, 0.1, and 0.15°C.

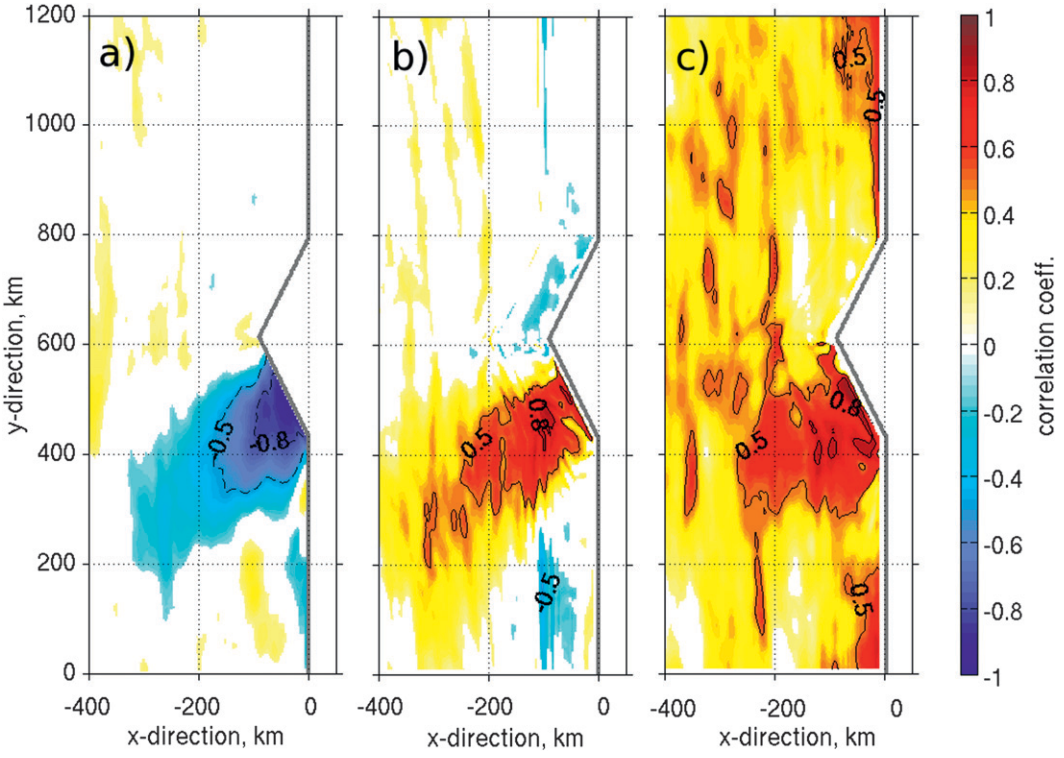

FIG. 11. Correlations between the time series of the diurnal anomalies of the (a) wind stress and surface pressure, (b) wind stress and SST, and (c) wind stress and 20-m depth average ocean current. Anomalies are computed by subtracting the corresponding 24-h running averages from the modeled data. Only significant correlations ($p < 0.05\%$) are shown and shaded.

period is 10 days (hours 37–276 of the forecast). The CWSST is defined as the quantity $|\nabla \mathrm{SST}| \sin\Delta\theta$, and DWSST as $|\nabla \mathrm{SST}| \cos\Delta\theta$, where $\Delta\theta$ is the angle between the wind stress vector and the SST gradient vector. Hourly values of CWSST and DWSST were computed from SST output and hourly averaged wind stresses, and then averaged over the 10-day period.

Major spatial structures of the derivative fields are found within 50–100 km of the coastline (Figs. 12b and 12c). The upwind region features good agreement between the corresponding wind stress and SST derivatives in their offshore extent and the sign (positive or negative), except within a few tens of kilometers of the tip of the cape. The downwind region features areas of strong signals of both positive and negative wind stress curl and divergence fields, which, however, are not in accordance with the corresponding SST gradients. A coastal band of convergence and higher wind stress curl is reestablished farther downstream, similar to the upstream values; the same is true for the coastal pattern of the SST gradients. The major result of the average derivative fields analysis is thus similar to those of the wind stress–SST: strong interconnections between the pairs of variables are found in the nearshore area within 50–100 km of the upwind region, whereas smaller-scale structures of the fields in the downwind region are not tightly connected to the shoreline, with little correspondence between the average fields.

To quantify the relationships between the average wind stresses, SSTs, and their derivatives, scatterplots and linear fits for the time-averaged fields are presented in Fig. 13; separate plots are shown for upwind and downwind regions. The data used are limited to grid points within 100 km of the coastline to focus on the upwelling zone where the field variations are the strongest; two nearshore ocean grid points were excluded to avoid the effects of numerical diffusion. Wind stress–SST relationships (Fig. 13a) show a slope of $0.021°\mathrm{C}\ (\mathrm{N\ m^{-2}})^{-1}$ for the upwind region, with relatively moderate scatter about the linear fit line. The downwind region shows large scatter of the data, with the resulting slope coefficient being close to 0.

In linear fits of the wind stress curl versus CWSST and wind stress divergence versus DWSST (Figs. 13b and 13c), the slope of a regression line is often referred to as the coupling coefficient. The upwind region yields slopes of 1.68 and 0.96, for wind stress curl–CWSST and wind stress divergence–DWSST, respectively, and both show

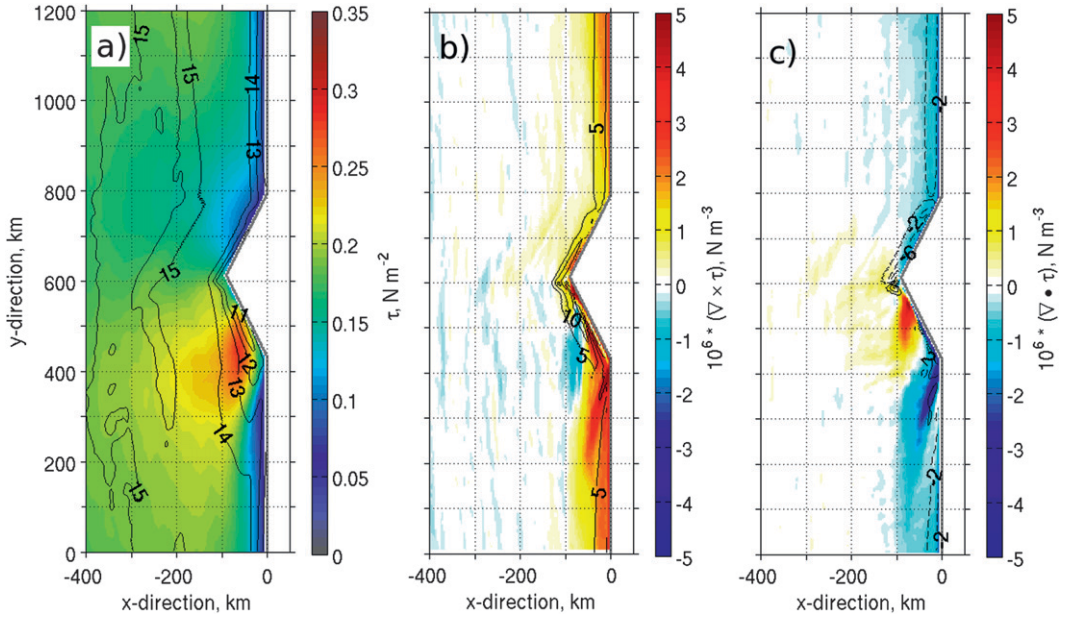

FIG. 12. (a) Wind stress (color, N m^{-2}) and SST (contours, °C) averaged for 10 days, from the coupled simulation; (b) wind stress curl (color, 10^6 N m^{-3}) and crosswind SST gradient [contour intervals 5°C (100 km)$^{-1}$]; (c) wind stress divergence (colors, 10^6 N m^{-3}) and downwind SST gradient [contour intervals 4°C (100 km)$^{-1}$], for the same time period.

relatively little scatter about the regression line. For the downwind region, the wind stress curl–CWSST coupling coefficient is slightly lower than for the upwind region (1.37), but features large scatter. The resulting negative coefficient for the wind stress divergence–DWSST (−3.44) is due to extensive scatter and few DWSST variations across the area. These results confirm our earlier findings that the orographic effects disrupt the average correlation between the average wind stresses and SSTs, as well as between their corresponding derivatives, on the lee side of the cape.

Estimation of coupling coefficients and temporal correlations between SST–wind stress pairs, derived from real-data COAMPS model forecasts, was recently presented by Haack et al. (2008). In their study, temporal correlations were computed between overlapping 29-day averages of wind stress derivatives and SST derivatives from real data, and they found negative correlations downwind of all major capes and headlands along the southern Oregon–California coast. This is consistent with our finding of reduced wind stress–SST coupling on the lee side of the cape. Our wind stress curl–CWSST coupling coefficient for the upwind and downwind regions combined (1.67) is within 20% of their real-data estimates (1.39) for a 100-km coastal swath. However, the wind stress divergence–DWSST coupling ratio for both regions in our study is negative (−0.33 versus their 1.37 estimate), which possibly results from the lack of spatial SST structure in the downwind direction.

b. *Simulation with fixed SST at the atmospheric lower boundary*

In the coupled case, upwelling generates reduced wind stress over the colder water adjacent to the coast. Nearshore winds are also affected by the coastal terrain and diurnal forcing, which may result in substantial wind stress gradients as well. To separate these effects from those of the upwelling, we conducted a second experiment by simulating a case with SST held invariant in time and space and at a fixed initial value (14°C), thus eliminating ocean feedback to the atmosphere. Since the differences in wind stress fields in these two cases can result only from the evolution of the SST in the coupled case, comparison of the cases could provide a convenient framework for analyzing the wind stress–SST interaction.

Average wind stress magnitudes in the fixed-SST case are shown in Fig. 14a, and average differences of hourly wind stresses and SSTs between the control case and fixed-SST case are shown in Fig. 14b. The wind stress field is qualitatively similar to that of the control case, featuring an area of stronger wind stresses on the lee side of the cape. Higher wind stresses, however, are found within 100–200 km along the entire coastline in the fixed-SST case, as is also indicated by the difference field, while the highest differences occur in the downwind region. Average wind

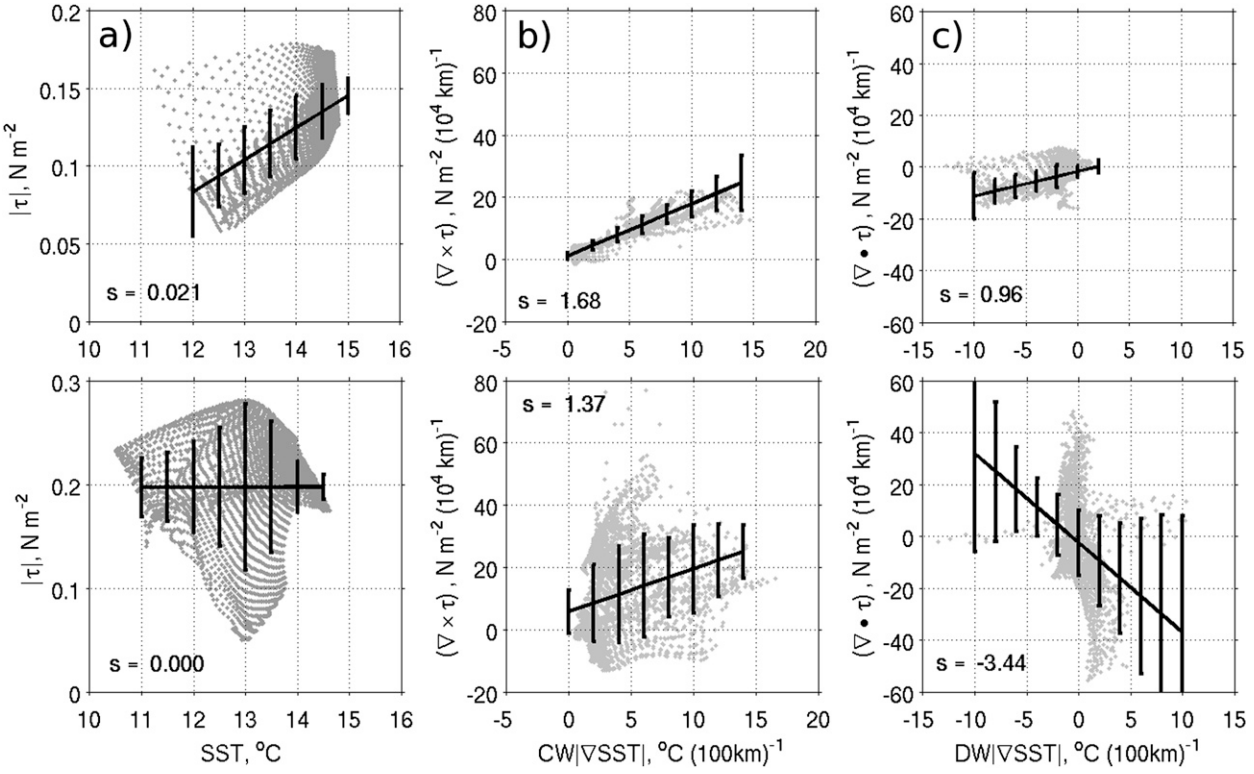

FIG. 13. Scatterplot and linear fit between the 10-day-averaged quantities from the coupled simulation, within the 200–km offshore region: (a) wind stress vs SST, (b) wind stress curl vs CWSST, and (c) wind stress divergence vs DWSST gradient. Points in the (top) ''upwind region'' (400 km north of the cape) and (bottom) ''downwind region'' (400 km south of the cape). All calculations are limited to the points within 100 km off the coast. Error bars denote standard deviations. Note that the data series have not been demeaned, in order to allow estimation of the standard deviations vs nominal values of the variables. The coupling coefficients remained identical when the data series were demeaned.

stress magnitude differences between the two cases correspond well with the SST differences: negative values are commonly found in both quantities inshore of the upwelling front [within ~(50–100) km of the coast], and positive values are identified beyond ~200 km off the coast. The area of negative SST differences on the lee side of the cape corresponds to the wider upwelling region in the coupled case. An area of positive SST differences results about 150 km offshore along the windward side of the cape (Fig. 14b), which is the upstream edge of the change in ocean bottom topography, for the open-ocean–continental shelf break transition. It is likely that the southward oceanic flow adjustment on the upstream side of this bathymetric feature affects the SSTs in the coupled case.

Study of the wind stress–SST coupling from their derivatives could be done similarly to the coupled case, but by using the average differences data. The average differences in wind stress curl and wind stress divergence between the coupled and fixed-SST cases are shown in Fig. 15; the overlaid contours are the ''differences'' in CWSST and DWSST between the same cases. Note that due to the fixed-SST case being spatially uniform, both CWSST and DWSST are zero. Thus, the differences in CWSST and DWSST in Fig. 15 are solely determined by their corresponding values from the coupled case. Higher wind stress curl (convergence) results in the coupled case being within 50 km of the coast in the upwind region, as evidenced by positive (negative) differences, and the correspondence with SST derivative fields is also high in that area for both pairs. The visual correspondence of the differences in the downwind region of the wind stress curl–CWSST and wind stress divergence–DWSST pairs is worse than in the upwind region, but shows considerable improvement compared to those from the coupled case (Figs. 12b and 12c).

Scatterplots and linear fits for the three pairs of differences are shown in Fig. 16, separately for the two regions (100 km inshore). A consistent response of the wind stress to SST changes is seen for the upwind region, resulting in an increase of about 0.12 N m^{-2} in wind stress per 10°C of temperature change. This response is weaker (0.08 N m^{-2} per 10°C) for the downwind region and is characterized by higher scatter. The wind stress curl–CWSST difference plot yields coefficients of 1.41 and 0.47 for the upwind and

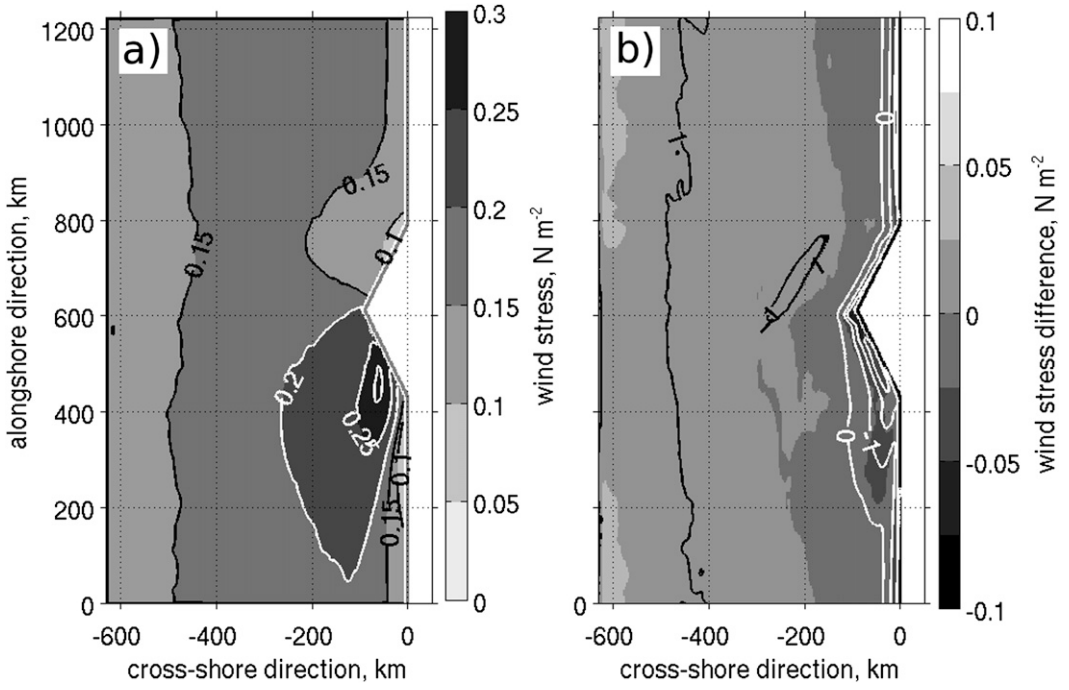

FIG. 14. (a) Wind stress (N m^{-2}) from the fixed-SST simulation, averaged for 10 days and (b) average differences in wind stresses (shading, N m^{-2}) and average differences in SST (contours, °C) between the coupled and fixed-SST cases. Contour intervals for the SST differences are 1°C, and are black for positive values and white for 0 and negative values.

downwind regions, respectively, and high scatter of the values in the downwind region. The coefficients for the wind stress divergence–DWSST differences are closer for the two regions, 1.40 and 1.20 for the upwind and downwind region, respectively. High scatter in the downwind region, however, in some way reduces the significance of the resulting higher value. Thus, as follows from the analysis of the time-averaged differences between the coupled and fixed-SST cases, wind stress–SST correlations are weaker on the lee side of the cape than on the windward side.

5. Summary and discussion

This study describes and analyzes coupled ocean–atmosphere mesoscale model simulations of the coastal circulation in regions of orographically intensified flow during the development of coastal upwelling. The model domain simulates an eastern ocean boundary with a single cape protruding into the ocean in the center of the coastline. This setting resembles the U.S. west coast, where northerly or northwesterly atmospheric flow is often found to produce a sequence of wind intensification regions downwind of major capes and points. When such a flow persists over a longer period, as during summertime conditions, it also causes nearshore ocean Ekman divergence, resulting in coastal upwelling. Our coupled simulation lasted for 11.5 days, and included both diurnal effects and multiday upwelling development. The model simulates the region of strong average wind stresses on the downwind side of an idealized cape, corresponding to a distinct lee-side trough formed over the coastal ocean in that area. A weak pressure ridge is found on the windward side of the cape as well. Modeled cloud regimes compared well with typical conditions, reflecting the formation of a cloud-free region behind the cape and cloud buildup on the upwind side of the cape and windward slopes of the coastal topography. A vertical cross section in the alongshore direction of the 10-day average pressure perturbation indicates that the vertical extent of the pressure decrease (increase) on the lee (windward) side of the cape is limited by the subsidence inversion.

The average atmospheric flow reflects the formation of an elevated southward jet on the lee side of the cape, peaking at the base of a temperature inversion; this jet weakens southward with the distance from the tip of the cape. A rapid downstream and shoreward decrease in the modeled boundary layer height is found on the downwind side near the tip of the cape. It is associated with the formation of a low-level temperature inversion, where supercritical flow is diagnosed. Formation of such an inversion in the leeward of the cape is likely

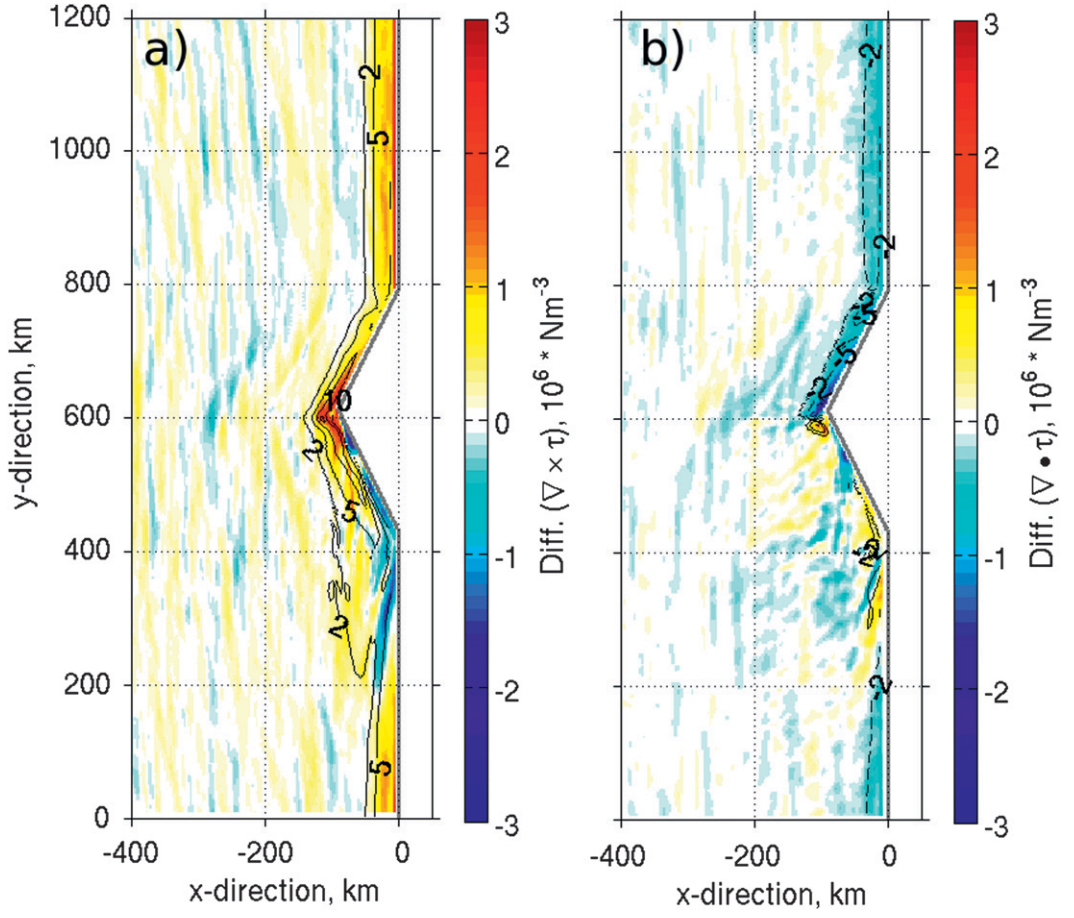

FIG. 15. Ten-day-average differences between the coupled and fixed-SST simulations in (a) wind stress curl (colors, 10^6 N m^{-3}) and crosswind SST gradients [contours, °C (100 km)$^{-1}$] and (b) wind stress divergence (colors, 10^6 N m^{-3}) and downwind SST gradient [contours, °C (100 km)$^{-1}$].

caused by the average easterly winds bringing warm air masses originating over land, and likely air warming during adiabatic decent behind the topographic obstacle. The mountain leeside dynamics modulated by the differential diurnal heating is thus found to dominate the wind regime in that area.

Observations of a smaller-scale leeside low or trough pose a great challenge, especially so over the coastal ocean. Application of mesoscale atmospheric models makes it possible to study such a phenomenon found in different coastal regimes, such as in a study by Davis et al. (2000) of the Catalina eddy, or a study by Batt et al. (2002) of the lee trough over eastern Tasmania. The dynamics of the leeside trough formed in our simulations could be similar to those of the Catalina eddy off Southern California, especially considering the comparable summertime conditions along the U.S. west coast.

Wind stress and surface pressure are found to undergo significant diurnal variability. Moreover, the coastal ocean is found to experience diurnal changes on the lee side of the cape, spatially corresponding to the area of strongest wind stresses: high significant correlations (over 0.5) of diurnal scale signals are found between wind stresses and SSTs, wind stresses, and surface depth-averaged ocean currents. The general realism of the strong diurnal cycle of the coastal winds is supported by observations and simulations from earlier studies (Haack et al. 2001; Kindle et al. 2002). The presence of strong diurnal modulation in the vertical structure of the atmospheric boundary layer wind in the coastal zone was also reported by Burk and Thompson (1996) and Bielli et al. (2002). In another study by Haack et al. (2001), real-data COAMPS forecasts were used to investigate the summertime marine layer flow between Cape Blanco, Oregon, and Cape Mendocino, California. In these real-data forecasts, the outer mesh boundary conditions were updated using atmospheric fields from the Navy Operational Global Atmospheric Prediction System (NOGAPS) model. The study found that supercritical flow features and their degree of interaction

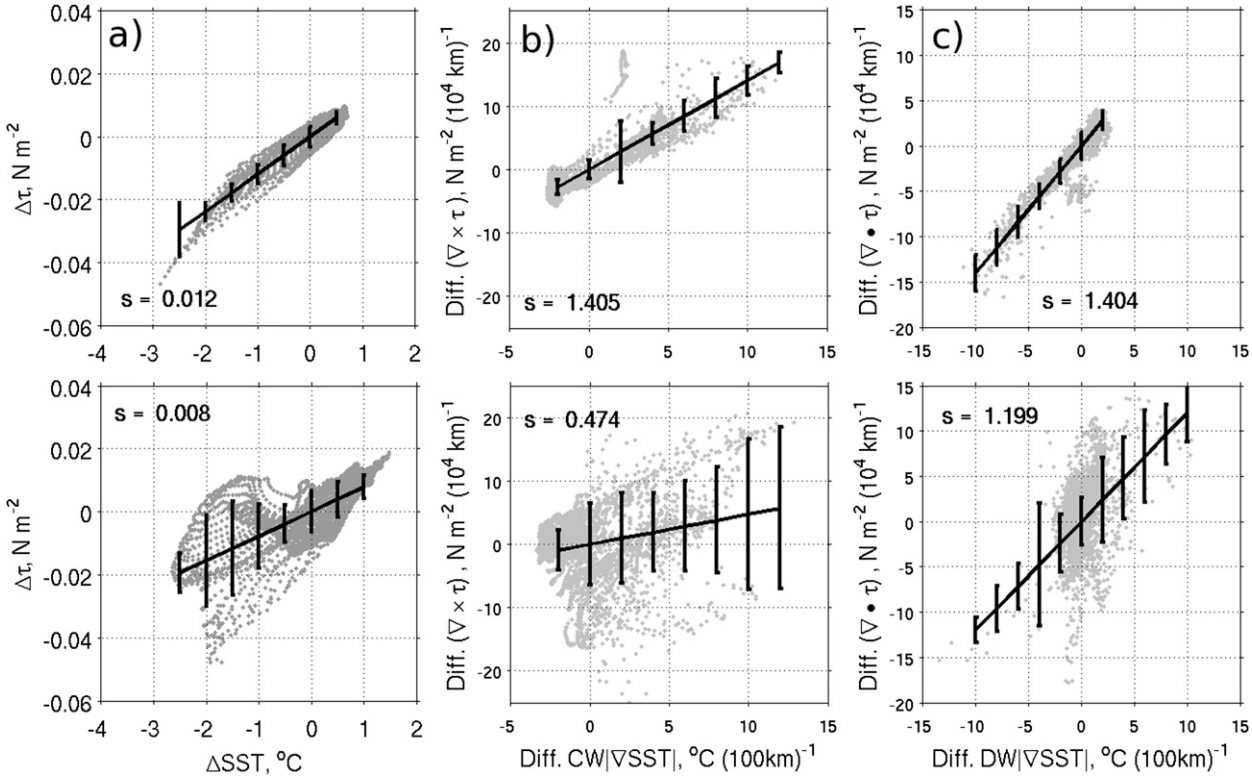

FIG. 16. Scatterplot and linear fit for the time-averaged differences between the coupled simulation and the fixed-SST simulation of the following quantities: (a) wind stress vs SST, (b) wind stress curl vs CWSST, and (c) wind stress divergence vs DWSST gradient. Points are shown from the (top) upwind (bottom) downwind regions. All calculations are limited to the points within 100 km off the coast.

vary diurnally. These diurnal oscillations may enhance or diminish the expansion fan in the lee of Cape Blanco. Our study demonstrates a strong diurnal cycle on the lee side of an idealized cape. Wind stresses are strongest and show their greatest spatial gradients during local evening, when the lee trough is the deepest; this area of wind intensification almost disappears in the local morning, during the time of maximum relaxation of the lee trough.

Simulated coastal upwelling produced an inshore decrease in SST up to 4°C, whereas offshore temperatures increased up to 2°C due to solar heating. The upwelling front was found about 50 km off the coast upwind of the cape. The offshore extent of the upwelling front doubled in width on the lee side of the cape, where the lowest nearshore SSTs are found. Negative surface fluxes produced over the coldest SSTs contributed to the increased static stability of the lower-tropospheric flow, which was marked by a rapid decrease in the atmospheric TKE.

Our study of the average air–sea coupling effects is based on estimating the relationships between temporal mean quantities and includes several techniques. First, wind stresses and their derivatives from the coupled case are analyzed and compared with the corresponding SSTs and its derivatives from the same simulation. An additional simulation with fixed SSTs is conducted in order to isolate the effects of ocean coupling, by eliminating an ocean feedback to the atmosphere. The temporal means of the modeled quantities from the coupled simulations are analyzed as follows: wind stress is mapped versus average SST for the 100-km coastal area, then similarly for the average wind stress curl versus average crosswind SST gradient (CWSST) and for the wind stress divergence versus downwind SST gradient (DWSST). Linear regression slopes, or coupling coefficients, are calculated separately for the upwind region and downwind region, 400 km north or south of the tip of the cape, respectively. The SST–wind stress coupling is spatially consistent and the coefficients are high in the upwind region, while a significant decrease in coupling results for the downwind region, characterized by high scatter of the data and smaller or negative coefficients. Higher scatter of the values in the expansion fan area supported the assumption of reduced average correlations in that region. This hypothesis is supported by a similar analysis of real-time forecasts of the U.S. west coast by Haack et al. (2008), reporting low or negative correlations between the low-pass-filtered wind stresses and SST data downwind of major capes.

Correlations between the time series of differences in SST and differences in wind stress, between the coupled and fixed-SST cases, confirmed previous findings on their strong relationship within the upwelling zone in the upwind region, and lower correlations on the lee side of the cape. Our estimations of the modeled wind stress change relative to the SST change indicated an average reduction of 0.12 N m^{-2} in wind stress per 10°C of SST decrease.

A major result of this study is that orographic and diurnal modulations of the near-surface atmospheric flow on the lee side of the cape strongly affect the wind stress dependence on the underlying SST conditions. A dynamic leeside trough is found to form downwind of the cape, whose diurnal modulations highly correlate with the wind stress anomalies. The region of dynamic wind stresses indicates an enhanced upper-ocean response to the atmospheric forcing on a diurnal scale. However, an average wind stress–SST coupling estimated from time-averaged fields shows weak coupling on the lee side of the cape. Upwind of the cape, air–sea coupling appears to be strong, enhanced by the dynamic response of the atmosphere to the coastal upwelling. The study suggests that the use of a fully coupled model in the nearshore zone with coastal promontories is necessary to adequately resolve air–sea coupling effects that appear to be strongly dependent on both the orographic and diurnal forcings.

Subsequent publications focused on these coupled results are expected to detail the boundary momentum and stability budgets and address the role of the local pressure gradient, including its spatial and temporal variabilities, on the wind regime in the vicinity of coastal capes. A separate publication is also planned for the ocean model analysis, the role of diurnal modulations, and the ocean feedback to the atmosphere on the resulting coastal circulation about the irregular coastline.

Acknowledgments. This research has been supported by Office of Naval Research Grant N00014-08-1-0933. This work has also been supported in part by a grant of computer time from the DoD High Performance Computing Modernization Program at the Maui High Performance Computing Center.

REFERENCES

Bane, J. M., M. D. Levine, R. M. Samelson, S. M. Haines, M. F. Meaux, N. Perlin, P. M. Kosro, and T. Boyd, 2005: Atmospheric forcing of the Oregon coastal ocean during the 2001 upwelling season. *J. Geophys. Res.,* **110,** C10S02, doi:10.1029/2004JC002653.

Barth, J. A., and R. L. Smith, 1998: Separation of a coastal upwelling jet at Cape Blanco, Oregon, USA. *S. Afr. J. Mar. Sci.,* **19,** 5–14.

——, S. D. Pierce, and R. L. Smith, 2000: A separating coastal upwelling jet at Cape Blanco, Oregon, and its connection to the California Current System. *Deep-Sea Res.,* **47,** 783–810.

Batt, K., L. Qi, and R. Morison, 2002: The modeling and observation of a lee trough event over eastern Tasmania. *Meteor. Atmos. Phys.,* **80,** 177–187.

Beardsley, R. C., C. E. Dorman, C. A. Friehe, L. K. Rosenfeld, and C. D. Winant, 1987: Local atmospheric forcing during the Coastal Ocean Dynamics Experiment. 1. A description of the marine boundary layer and atmospheric conditions over a northern California upwelling region. *J. Geophys. Res.,* **92,** 1467–1488.

Bielli, S., P. L. Barbour, R. M. Samelson, E. Skyllingstad, and J. Wilczak, 2002: Numerical study of the diurnal cycle along the central Oregon coast during summertime northerly flow. *Mon. Wea. Rev.,* **130,** 992–1008.

Burk, S. D., and W. T. Thompson, 1996: The summertime low-level jet and marine boundary layer structure along the California coast. *Mon. Wea. Rev.,* **124,** 668–686.

——, and T. Haack, 2000: The dynamics of wave clouds upwind of coastal orography. *Mon. Wea. Rev.,* **128,** 1438–1455.

——, ——, and R. M. Samelson, 1999: Mesoscale simulation of supercritical, subcritical, and transcritical flow along coastal topography. *J. Atmos. Sci.,* **56,** 2780–2795.

Castelao, R., and J. A. Barth, 2007: The role of wind stress curl in jet separation at a cape. *J. Phys. Oceanogr.,* **37,** 2652–2671.

Chelton, D. B., 2005: The impact of SST specification on ECMWF surface wind stress fields in the eastern tropical Pacific. *J. Climate,* **18,** 530–550.

——, and Coauthors, 2001: Observations of coupling between surface wind stress and sea surface temperature in the eastern tropical Pacific. *J. Climate,* **14,** 1479–1498.

——, M. G. Schlax, and R. M. Samelson, 2007: Summertime coupling between sea surface temperature and wind stress in the California Current System. *J. Phys. Oceanogr.,* **37,** 495–517.

Davis, C., S. Low-Nam, and C. Mass, 2000: Dynamics of a Catalina eddy revealed by numerical simulation. *Mon. Wea. Rev.,* **128,** 2885–2904.

Dorman, C. E., T. Holt, D. P. Rogers, and K. Edwards, 2000: Large-scale structure of the June–July 1996 marine boundary layer along California and Oregon. *Mon. Wea. Rev.,* **128,** 1632–1652.

Edwards, K. A., A. M. Rogerson, C. D. Winant, and D. P. Rogers, 2001: Adjustment of the marine atmospheric boundary layer to a coastal cape. *J. Atmos. Sci.,* **58,** 1511–1528.

——, D. P. Rogers, and C. E. Dorman, 2002: Adjustment of the marine atmospheric boundary layer to the large-scale bend in the California coast. *J. Geophys. Res.,* **107,** 3213, doi:10.1029/2001JC000807.

Enriquez, A. G., and C. A. Friehe, 1995: Effects of wind stress and wind stress curl variability on coastal upwelling. *J. Phys. Oceanogr.,* **25,** 1651–1671.

Fairall, C. W., E. F. Bradley, D. P. Rogers, J. B. Edson, and G. S. Young, 1996: Bulk parameterization of air–sea fluxes for Tropical Ocean Global Atmosphere Coupled Ocean–Atmosphere Response Experiment. *J. Geophys. Res.,* **101,** 3747–3764.

Haack, T., S. D. Burk, C. E. Dorman, and D. P. Rogers, 2001: Supercritical flow interaction within the Cape Blanco–Cape Mendocino orographic complex. *Mon. Wea. Rev.,* **129,** 688–708.

——, ——, and R. M. Hodur, 2005: U.S. West Coast surface heat fluxes, wind stress, and wind stress curl from a mesoscale model. *Mon. Wea. Rev.,* **133,** 3202–3216.

——, D. Chelton, J. Pullen, J. Doyle, and M. Schlax, 2008: Air–sea interaction from U.S. west coast summertime forecasts. *J. Phys. Oceanogr.,* **38,** 2414–2437.

Harshvardhan, R., D. A. Davies, Randall, and T. G. Corsetti, 1987: A fast radiation parameterization for atmospheric circulation models. *J. Geophys. Res.,* **92** (D1), 1009–1016.

Hodur, R. M., 1997: The Naval Research Laboratory's Coupled Ocean–Atmosphere Mesoscale Prediction System (COAMPS). *Mon. Wea. Rev.,* **125,** 1414–1430.

Holton, J. R., 1992: *An Introduction to Dynamic Meteorology*. 3rd ed. Academic Press, 511 pp.

Huyer, A., J. H. Fleischbein, J. Keister, P. M. Kosro, N. Perlin, R. L. Smith, and P. A. Wheeler, 2005: Two coastal upwelling domains in the Northern California Current. *J. Mar. Res.,* **63,** 901–929.

Jin, X., C. Dong, J. Kurian, J. C. McWilliams, D. B. Chelton, and Z. Li, 2009: SST–wind interaction in coastal upwelling: Oceanic simulation with empirical coupling. *J. Phys. Oceanogr.,* **39,** 2957–2970.

Kindle, J. C., R. M. Hodur, S. deRada, J. Paduan, L. Rosenfeld, and F. Chavez, 2002: A COAMPS reanalysis for the eastern Pacific: Properties of the diurnal sea breeze along the central California coast. *Geophys. Res. Lett.,* **29,** 2203–2207.

Klemp, J. B., and R. B. Wilhelmson, 1978: The simulation of three-dimensional convective storm dynamics. *J. Atmos. Sci.,* **35,** 1070–1096.

Koračin, D., and C. Dorman, 2001: Marine atmospheric boundary layer divergence and clouds along California in June 1996. *Mon. Wea. Rev.,* **129,** 2040–2055.

Larson, J., R. Jacob, and E. Ong, 2005: The Model Coupling Toolkit: A new Fortran 90 toolkit for building multiphysics parallel coupled models. *Int. J. High Perform. Comput. Appl.,* **19,** 277–292.

Lin, Y.-L., R. D. Farley, and H. D. Orville, 1983: Bulk parameterization of the snow field in a cloud model. *J. Climate Appl. Meteor.,* **22,** 1065–1092.

Louis, J.-F., M. Tiedtke, and J.-F. Geleyn, 1982: A short history of the operational PBL parameterization of ECMWF. *Proc. Workshop on Planetary Boundary Layer Parameterization,* Shinfield Park, Reading, United Kingdom, ECMWF, 59–79.

McKendry, I. G., A. P. Sturman, and I. F. Owens, 1986: A study of interacting multi-scale wind systems, Canterbury plains, New Zealand. *Meteor. Atmos. Phys.,* **35,** 242–252.

Mellor, G. L., and T. Yamada, 1974: A hierarchy of turbulence closure models for planetary boundary layers. *J. Atmos. Sci.,* **31,** 1791–1806.

Miller, M. J., and A. J. Thorpe, 1981: Radiation conditions for the lateral boundaries of limited-area numerical models. *Quart. J. Roy. Meteor. Soc.,* **107,** 615–628.

Oertel, H., and L. Prandtl, 2004: *Prandtl's Essentials of Fluid Mechanics*. Springer, 723 pp.

Perlin, N., R. M. Samelson, and D. B. Chelton, 2004: Scatterometer and model wind and wind stress in the Oregon–northern California coastal zone. *Mon. Wea. Rev.,* **132,** 2110–2129.

——, E. D. Skyllingstad, R. M. Samelson, and P. L. Barbour, 2007: Numerical simulation of air–sea coupling during coastal upwelling. *J. Phys. Oceanogr.,* **37,** 2081–2093.

Rogerson, A. M., 1999: Transcritical flows in the coastal marine atmospheric boundary layer. *J. Atmos. Sci.,* **56,** 2761–2779.

Rutledge, S. A., and P. V. Hobbs, 1983: The mesoscale and microscale structure and organization of clouds and precipitation in midlatitude cyclones. VIII: A model for the ''seeder–feeder'' process in warm-frontal rainbands. *J. Atmos. Sci.,* **40,** 1185–1206.

Samelson, R. M., 1992: Supercritical marine layer flow along a smoothly varying coastline. *J. Atmos. Sci.,* **49,** 1571–1584.

——, and Coauthors, 2002: Wind stress forcing of the Oregon coastal ocean during the 1999 upwelling season. *J. Geophys. Res.,* **107,** 3034, doi:10.1029/2001JC000900.

Shchepetkin, A. F., and J. C. McWilliams, 2005: The Regional Ocean Modeling System (ROMS): A split-explicit, free-surface, topography-following-coordinate oceanic model. *Ocean Modell.,* **9,** 347–404.

Skyllingstad, E. D., R. M. Samelson, L. Mahrt, and P. Barbour, 2005: A numerical modeling study of warm offshore flow over cool water. *Mon. Wea. Rev.,* **133,** 345–361.

——, D. Vickers, L. Mahrt, and R. M. Samelson, 2007: Effects of mesoscale sea-surface temperature fronts on the marine boundary layer. *Bound.-Layer Meteor.,* **123,** 219–237.

Song, Q., D. B. Chelton, S. K. Esbensen, N. Thum, and L. W. O'Neill, 2009: Coupling between sea surface temperature and low-level winds in mesoscale numerical models. *J. Climate,* **22,** 146–164.

Strub, P. T., P. M. Kosro, and A. Huyer, 1991: The nature of the cold filaments in the California Current System. *J. Geophys. Res.,* **96** (C8), 14 743–14 768.

Sturman, A. P., and P. D. Tyson, 1981: Sea breezes along the Canterbury coast in the vicinity of Christchurch, New Zealand. *Int. J. Climatol.,* **1,** 203–219.

Vickers, D., L. Mahrt, J. Sun, and T. Crawford, 2001: Structure of offshore flow. *Mon. Wea. Rev.,* **129,** 1251–1258.

Wang, S., Q. Wang, and J. Doyle, 2002: Some improvements to Louis surface flux parameterization. Preprints, *15th Conf. on Boundary Layer and Turbulence,* Wageningen, Netherlands, Amer. Meteor. Soc., 13.3A. [Available online at http://ams.confex.com/ams/pdfpapers/44519.pdf.]

Warner, J. C., N. Perlin, and E. D. Skyllingstad, 2008: Using the Model Coupling Toolkit to couple earth system models. *Environ. Model. Software,* **23,** 1240–1249.

Winant, C. D., C. E. Dorman, C. A. Friehe, and R. C. Beardsley, 1988: The marine layer off northern California: An example of supercritical channel flow. *J. Atmos. Sci.,* **45,** 3588–3605.